

**Department of Physics and Astronomy  
University of Heidelberg**

Bachelor Thesis in Physics  
submitted by

**Mathurin Arthur Choblet**

born in Lich (Germany)

**2019**



# **Creation of structured light for investigating optical nonlinearities in a Rydberg gas**

This Bachelor Thesis has been carried out by Mathurin Arthur Choblet at the  
Physikalisches Institut in Heidelberg  
under the supervision of  
Prof. Matthias Weidemüller



Grau, teurer Freund, ist alle Theorie,  
und grün des Lebens goldner Baum.

— Mephistopheles in Faust I, Goethe



## ABSTRACT

---

The use of structured light in Rydberg gases opens up new possibilities for investigating optical nonlinearities. In order to create structured light, a spatial light modulator (SLM) is used to imprint phase patterns onto a light beam, which modulates the intensity of light in the Fourier plane. First, the phase patterns are computed using enhanced iterative Fourier transform algorithms. Second, these phase patterns are tested in an experimental setup. In spite of the simulations being highly accurate, optical aberrations have to be accounted for. The corrective Shack-Hartmann algorithm is implemented to correct these aberrations, and additional noise sources are identified. My thesis investigates these two central aspects. Further considerations that might be used to optimise the setup subsequently to this work are presented.

## ZUSAMMENFASSUNG

---

Die Verwendung von strukturiertem Licht in Rydberg Gasen eröffnet neue Möglichkeiten für die Untersuchung optischer Nichtlinearitäten. Zu diesem Zwecke benutzen wir einen räumlichen Lichtmodulator, welcher die Phase von Licht und somit in der Fourierebene die Intensität modulieren kann. Zunächst werden die Phasenverteilungen zur Manipulation des Lichts mittels iterativer Fourier-Transformations Algorithmen berechnet. Des Weiteren müssen diese Phasenverteilungen in einem optischen Aufbau getestet werden, da Störungen im optischen Aufbau die feinstrukturierten Intensitätsverteilungen beeinträchtigen. Der Shack-Hartmann Algorithmus wird implementiert um diese Aberrationen zu korrigieren, außerdem werden weitere Fehlerquellen identifiziert. Meine Arbeit beschäftigt sich mit diesen zentralen Aspekten zur Erzeugung von strukturiertem Licht und beschreibt über das praktisch Umgesetzte hinaus eine Reihe von notwendigen Maßnahmen um die Qualität der Intensitätsverteilungen weiter zu verbessern.



## CONTENTS

---

<b>1</b>	<b>INTRODUCTION</b>	<b>1</b>
<b>2</b>	<b>THEORY</b>	<b>3</b>
<b>2.1</b>	Investigating optical nonlinearities with Rydberg atoms	3
<b>2.2</b>	Spatial Light Modulators . . . . .	9
<b>2.3</b>	Fourier Optics and Fraunhofer diffraction . . . . .	13
<b>3</b>	<b>GENERATION OF PHASE PATTERNS</b>	<b>23</b>
<b>3.1</b>	Holography . . . . .	23
<b>3.2</b>	Iterative Fourier transform algorithms . . . . .	24
<b>3.3</b>	Analytic beam shaping . . . . .	26
<b>4</b>	<b>THE MRAF-ALGORITHM</b>	<b>29</b>
<b>4.1</b>	The general idea . . . . .	29
<b>4.2</b>	Figures of merit . . . . .	30
<b>4.3</b>	The initial phase guess . . . . .	32
<b>4.4</b>	The input amplitude . . . . .	36
<b>4.5</b>	Reduction to a one-dimensional problem . . . . .	36
<b>4.6</b>	Conclusion and versatility demonstration . . . . .	38
<b>5</b>	<b>PRACTICAL IMPLEMENTATION AND MEASUREMENTS</b>	<b>43</b>
<b>5.1</b>	Optical setup . . . . .	43
<b>5.2</b>	Aberration correction with a Spatial Light Modulator .	44
<b>5.3</b>	Amplitude reconstruction in the SLM plane . . . . .	53
<b>5.4</b>	Experimental measurements . . . . .	54
<b>6</b>	<b>CONCLUSION</b>	<b>61</b>
<b>6.1</b>	Summary . . . . .	61
<b>6.2</b>	Outlook . . . . .	62
	<b>BIBLIOGRAPHY</b>	<b>69</b>



## INTRODUCTION

---

The development of quantum mechanics at the beginning of the last century can be considered a paradigm shift in science as coined by Kuhn [1]. While the theory of quantum mechanics relentlessly continued its triumph, the field of Rydberg atoms emerged as a vast playground for physicists to test the theory, its limits and how to extend it. Due to their high principal quantum number, Rydberg atoms have a variety of intriguing and extreme properties, namely an extreme controllability by external fields, strong long-range interactions and long lifetimes that opened a diverse field of research topics [2]: Ranging from ultra-long range molecules, investigations of few- and many-body physics, quantum information theory and phenomena of quantum optics, the research potential is far from being exhausted and the pace of developments is continuously increasing. Concerning quantum optics, a three-level system like a Rydberg gas can be used as a medium where, under appropriate conditions, the phenomenon of Electromagnetically Induced Transparency (EIT) can be observed, meaning that light will be able to traverse an otherwise opaque medium. This effect can be used to investigate phenomena of nonlinear optics. The Rydberg group at the Physikalisches Institut has focused its research on this nonlinear behaviour and the latest efforts have been dedicated to enhance optical nonlinearities with EIT in a Rydberg gas [3]. The latest proposal to further explore optical nonlinearities consists of measuring the response of a Rydberg gas to spatially resolved light. For reconstruction of the nonlinearity of the medium light patterns with an adjustable periodicity are required.

But how can light actually be shaped?

For centuries humankind perfected the use of tools like lenses, prisms, apertures and mirrors to guide and analyse light, although it was only the invention of the laser [4] and the concept of holography [5] that paved the way for taking the leap from analysis to synthesis. In the beginning, holography was realized using photographic emulsion plates, but the production of such plates is cumbersome. Moreover, the created light-fields are not reconfigurable, because the plates are only designed for one specific light intensity.

It took the development of spatial light modulators (SLMs) based on liquid crystal technology, a pinnacle of modern technology, to bring holography to the next level. In a phase-modulating SLM the optical path length is manipulated on an array of pixels, enabling

one to shape intensities in a far field according to Fraunhofer diffraction. As SLMs are reconfigurable, an optical setup does not need to be physically altered to create all kinds of light fields. Hence, they quickly became valuable for the enhancement of optical tweezers for microscopic particles in biology and chemistry [6]. The possible use of SLMs in atomic physics also didn't go unnoticed, as they can be used for shaping precise traps and robust potentials in quantum dynamic [7], and since then SLMs have become an integral component of experiments with ultracold quantum gases[8, 9]. Nonetheless, SLMs have so far not been used for observing nonlinear optics with structured light in Rydberg gases. Therefore, the experiment proposed by the Rydberg group presents a novel approach for the application of a spatial light modulator.

The proper control of a SLM is inextricably linked to the topic of computer-generated holography and the problem of phase retrieval. It turns out that calculating the necessary phase patterns for specific target intensities is a complicated issue with many different solutions. Since the 1970s a lot of research was pursued on these topics, e.g. on iterative Fourier transform algorithms, knowledge that is of high value for light shaping.

This report presents the subtleties of setting up a spatial light modulator, starting with the simulations of continuous phase patterns with an Iterative Fourier Transform Algorithm to the setup of the experimental test platform, where a range of issues like aberrations have to be tackled. In addition possible further improvements are discussed, and a work plan for the consequent steps towards implementing the SLM in the Rydberg atoms experiment is presented.

At this point I would like to acknowledge two sources that served as the main references for this thesis. The PhD thesis "Quantum Engineering with Ultracold Atoms" by Rick van Bijnen [8] contains a chapter where the use of a phase-modulating SLM is thoroughly depicted and many creative ideas to optimize it are presented. Marvin Holten from the Ultracold Quantum Gases group at the Physikalisches Institut kindly provided us with an original version of the LabVIEW-program to control the SLM, that he developed at the time of his bachelor thesis "Hamiltonian Engineering with Ultracold Atoms" [10], which also contains many valuable insights.

The Ultracold Quantum Gases group has since then developed an impressive command of beam shaping with a SLM, e.g. for the creation of rotating microtraps [9]. The Rydberg group will for sure be able to learn a lot from their experiences.

# 2

## THEORY

---

In order to explain the overarching goal of creating structured light, I begin by giving a short summary on investigating nonlinear optics with Rydberg atoms. Then the theoretical groundwork for understanding how to shape a laser beam using a spatial light modulator is laid, therefore the principles of a phase-modulating SLM are presented. Then the necessary basics of Fourier optics are derived, before applying the formulas to our SLM.

### 2.1 INVESTIGATING OPTICAL NONLINEARITIES WITH RYDBERG ATOMS

In this section an overview of the underlying theoretical concepts of Rydberg EIT is given and the necessity of using structured laser light for investigations of the optical nonlinearity is outlined. For Rydberg atoms and the concept of EIT a large number of publications provide an in-depth introduction. To gain deeper insights the reader may wish to read [11] about Rydberg atoms, [2] about recent developments of research with ultracold Rydberg atoms, [12, 13] about Electromagnetically Induced Transparency, [14] about nonlinear optics with Rydberg atoms and [3] from our group about the latest ideas to enhance these nonlinearities.

#### 2.1.1 *Rydberg atoms*

Atoms, where one of the electrons is excited to a high principal quantum number  $n$ , are called Rydberg atoms. This large principal quantum number has serious consequences for the basic properties of such atoms. For instance, in terms of the Bohr model for a one-electron system the orbital radius of the electron scales with  $n^2$ , which can be interpreted as the electron being far away from the atom's nucleus. In this picture it is comprehensible that this results in a high polarisability of these atoms, which is scaling with  $n^7$ . As a direct consequence of these exaggerated properties, atoms in a Rydberg state are very sensitive to external fields.

Nonetheless, solving the Schrödinger equation for atoms with more than one electron is impossible analytically, elementary hydrogen being the only atom where such a solution exists. Atoms that are similar to a one-electron-system are alkali metals, as they only have one

valence electron. Hence, the energy levels of alkali atoms can be calculated using an adapted hydrogen model taking into account the experienced charge of the core. This results in a quantum number being shifted by a specific quantum defect. In our experiment Rubidium-87 atoms are excited up to states with  $n$  ranging from 40 to 70.

For their quantum mechanical nature to appear, ensembles of Rydberg atoms have to be cooled down to a few micro Kelvin using cooling methods, a dipole trap and sophisticated magneto-optical trap. At these low temperatures the interaction energies will become more important than the kinetic energies. For more details on our current experiment the reader is referred to [3].

Rydberg atoms in our experiment can be described as a three-level system consisting of a ground state  $|g\rangle$ , an excited state  $|e\rangle$  and a Rydberg state  $|r\rangle$ . In our case the states  $|g\rangle$  and  $|e\rangle$  are coupled by a probe laser with frequency  $\omega_p$  and  $|e\rangle$  and  $|r\rangle$  by the control laser with frequency  $\omega_c$  (three-level ladder-scheme). The coupling strength between the quantum mechanical states is characterized by the Rabi frequency  $\Omega$ . It depends on the transition dipole moment  $\mathbf{d}$  and the driving field  $\mathbf{E}$ ,

$$\Omega = \frac{-\mathbf{d} \cdot \mathbf{E}}{\hbar}, \quad (1)$$

where  $\hbar$  is the Planck constant. Hence, the squared Rabi frequency  $\Omega^2$  is proportional to the intensity of the driving laser.

Because of the large polarisability of Rydberg atoms long-range interactions between Rydberg atoms occur. Performing a Taylor expansion of the energy of a two-Rydberg-atom system, it can be shown that dipole-dipole type and van der Waals type interactions arise [3]. The latter's potential scales with  $\frac{C_6}{R^6}$ , where  $R$  is the distance. As the van der Waals coefficient  $C_6$  scales with  $n^{11}$  this kind of interaction is highly tuneable by changing the  $n$  of the system with the coupling laser.

One prominent consequence of Rydberg-Rydberg interaction is the so called Rydberg blockade: Within a certain Rydberg blockade radius  $R_b$  only one and not both atoms can be excited into a Rydberg state. This can be explained in the pair state basis of such a system as shown in figure 1. This pair-state illustration shows that for short distances the energy level of the  $|rr\rangle$  pair states gets shifted due to the interaction, such that a transition from  $|rg\rangle$  to the doubly excited Rydberg state  $|rr\rangle$  is prohibited. Inside such a blockade sphere only one atom is allowed to be in a Rydberg state, thus all the others are effective two-level atoms.

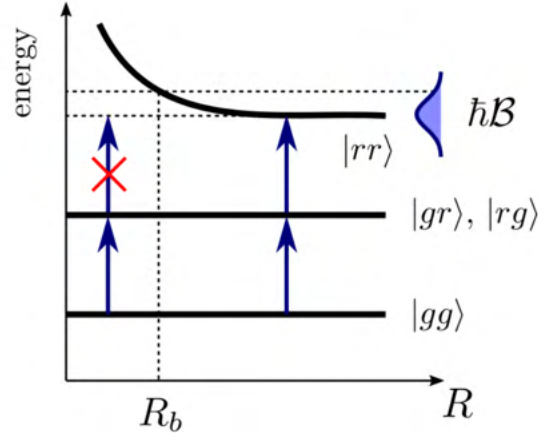


Figure 1: Depiction of the Rydberg blockade effect. The blockade radius  $R_b$  is emerging from the two atomic van der Waals interaction, which depends of the distance of the two interaction atoms  $R$ . Below a typical radius, the doubly excited state  $|rr\rangle$  cannot be reached by excitation of probe and control beam frequency any longer.  $B$  is the laser bandwidth, from [3].

### 2.1.2 Electromagnetically Induced Transparency (EIT)

In general, the response of an atomic medium to light depends on how the individual atoms are polarised by the electric light field. In order to define a macroscopic quantity for the polarisability of the medium the average dipole moment  $\langle d \rangle$ , that is induced per atom is introduced. The response of  $N$  atoms to an electric field  $E$  can be described by the complex valued electric susceptibility  $\chi$

$$\chi = \frac{N\langle d \rangle}{\epsilon_0 E}, \quad (2)$$

where  $\epsilon_0$  is the vacuum permittivity.

The susceptibility of a medium affects both absorption and refraction of light propagating through it. The imaginary part of  $\chi$  influences the absorption of light, the real part its diffraction as it introduces a phase difference. Therefore, a transparent medium exhibits a susceptibility with a zero imaginary part.

In quantum mechanical systems the susceptibility-situation is as follows: When a two-level system is excited by an excitation laser, where the detuning from the transition wavelength is zero, the imaginary part of  $\chi$  has a maximum (see figure 2), therefore light is absorbed. In a three-level system the situation can be completely different under the conditions of the states having a long lifetime and the coupling frequency  $\Omega_c$  being stronger than the probe frequency  $\Omega_p$ .

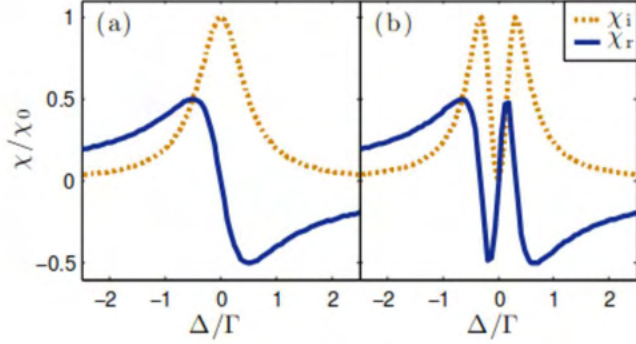


Figure 2: The real and imaginary part  $\chi_r$  and  $\chi_i$  of the susceptibility in a two-level system (a) and in a three-level EIT-system (b) as a function of the laser detuning  $\Delta$ , where  $\Gamma$  is the transition linewidth and  $\chi_0$  an normalization constant.  $\chi_r$  determines the diffraction  $\chi_i$  the absorption of light, hence a three-level EIT-system is rendered transparent at detuning zero, from [14].

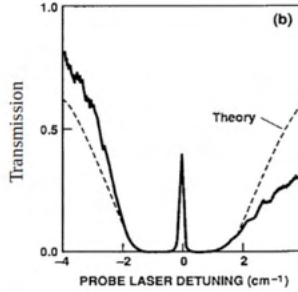


Figure 3: First observation of EIT measured in a Strontium gas by *Boller et al.* [15]. The transmission on the y-axis is plotted against the laser detuning, for a small detuning window the gas was rendered transparent, although the transmission at that point is zero for a two-level system.

Due to quantum interference effects, one transition can be effectively prohibited in a narrow frequency detuning window. The imaginary part of  $\chi$  becomes zero, resulting in full transparency instead of absorption. This effect was observed for the first time in a Strontium gas in 1991 [15], see figure 3. Another interesting effect is that for EIT conditions on single photon resonance (zero detuning) the real-part of  $\chi$  also vanishes with a steep gradient at that point. This strong dispersion can be used to extremely reduce the velocity of light. Using EIT *Hau et al.* slowed down light to 17m/s [16].

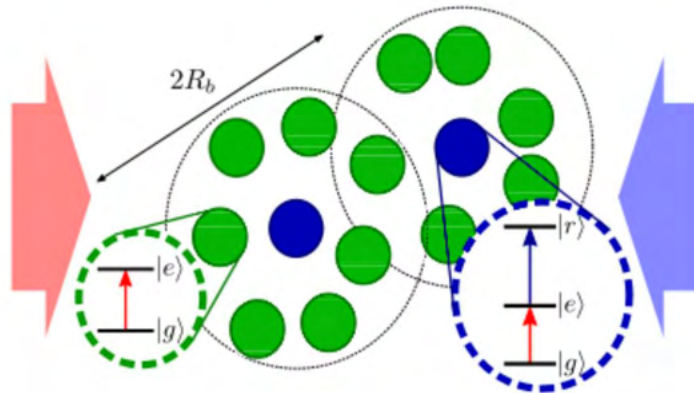


Figure 4: Scheme of the Rydberg-EIT situation. The probe laser (red arrow) excites the atoms such that they become two-level systems (green circles), some of the atoms are further excited into a Rydberg state by the coupling laser (blue arrow and blue atoms). Due to the Rydberg blockade their neighboring atoms remain effective two-level systems, from [3].

### 2.1.3 Nonlinear optics with Rydberg atoms

A Rydberg gas as an EIT-medium offers great opportunities for observing optical nonlinearities.

An optical nonlinearity is present when the susceptibility  $\chi$  depends on the amplitude of the external field. In this case  $\chi$  can be expanded in a power series of  $E$  [17]:

$$\chi = \chi^{(1)} + \chi^{(2)} \cdot E + \chi^{(3)} \cdot E^2 + \dots \quad (3)$$

In experiments with ultracold atoms,  $\chi^3$  is the first nonlinear term of interest due to the centrosymmetry of the gas.

The Rydberg blockade effect actually results in such an optical nonlinearity. As can be seen in figure 4 inside a Rydberg blockade sphere only one atom (blue) can be excited into a Rydberg state, while the surrounding atoms (green) are effective two-level systems. In this situation the electromagnetically induced transparency is reduced because the two-level atoms will couple to the probe beam (red). The fraction of atoms in a Rydberg state is proportional to  $\Omega_p^2$ . Hence, the absorption increases quadratically with the Rabi frequency of the probe laser, which is a signature of a third order nonlinear process.

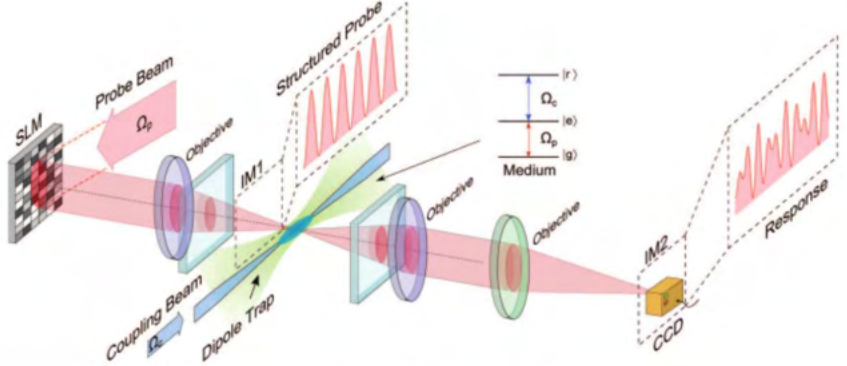


Figure 5: Proposed investigation of optical nonlinearities with structured light. The probe beam is modulated by a Spatial Light Modulator and then focused onto the cloud of Rydberg atoms with an objective. The induced response of the medium in form of a changed intensity distribution is recorded with a CCD-camera.

#### 2.1.4 Research plan

The Rydberg group aims to measure the transverse spatial structure of the nonlinear susceptibility  $\chi^{(3)}$ . In order to spatially resolve  $\chi^{(3)}$  structured probe light is going to be used. Here the response of the Rydberg medium for periodic intensity distributions with varying transversal length scales, called  $k_{\perp}$ -modes, will be measured, as illustrated in figure 5. From these measurements of  $\chi^{(3)}$  in Fourier space the spatial distribution  $\chi^{(3)}(\mathbf{r})$  can be deduced.

Simple patterns with a distinct  $k_{\perp}$ -mode could consist of sinuses, where the  $k_{\perp}$ -mode defines the peak to peak distance, for instance  $\sin^2(x)$  or  $\sin^2(y)$  (see figure 6). Furthermore, radial distributions of the form  $\sin^2(\sqrt{x^2 + y^2})$  are conceivable. We take the squared sinuses because the intensity of light cannot be negative. As the Rydberg blockade is an essential part of the nonlinearity, it is obvious that we would like the peak to peak distance to go down to the blockade radius which lies on a  $\mu\text{m}$ -scale.

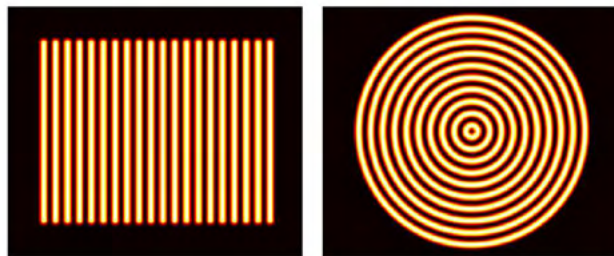


Figure 6:  $\sin^2(x)$  and  $\sin^2(r)/2$  target distributions that could be implemented into the Rydberg experiment.

## 2.2 SPATIAL LIGHT MODULATORS

As mentioned in the introduction, a large variety of methods to shape wavefronts has been developed over time, with Spatial light modulators being the most recent and innovative development. The term spatial light modulators actually comprises a range of devices that modulate the intensity of a laser beam, its phase or both at the same time. For an overview of the variety of existing SLM devices the reader may wish to read [18]. In this subsection only the details relevant for our phase-modulating liquid crystal on silicon (LCOS-) SLM<sup>1</sup> are discussed.

### 2.2.1 Liquid crystals and their birefringent properties

Since their discovery at the end of the 19<sup>th</sup> century, liquid crystals have become part of our every day life. They are a centrepiece of many types of electronic displays that are in use today.

The molecules in liquid crystals offer a variety of astonishing physical properties, hence their ambiguous name. On the one hand the molecules are seemingly free of movement such that they are reminiscent of liquids, but on the other hand they can show a particular order on a macro- or microscopic scale. The study of liquid crystals form a distinct research field and are extensively treated in numerous textbooks like [19]. We are going to make use of their ability to be specifically aligned by an external electric field.

Typical arrangements of the liquid crystals molecules are referred to as phases, in the present case the optical properties of the *parallel-aligned nematic phase* are used. Such a nematic phase is sketched in figure 7a, the rod-like molecules show a long-range order in form of a parallel alignment of the molecules, but the positions are not fixed. As a consequence such a medium is anisotropic.

In a LCOS-SLM this initial arrangement of the molecules is imposed by the direction of fine polishing the glass plates, which represents the boundary conditions (see 7b).

The fundamental property necessary for phase-modulation is the birefringence of these nematic phase liquid crystals. In general light travelling through a birefringent medium experiences two refractive indices, depending on the plane of incidence and the polarization. This phenomenon is depicted by dissecting the light ray in one part that travels along the extraordinary axis with a refractive index  $n_e$  and one traveling along the ordinary axis with  $n_o$ . The axis with the larger refraction index is also called slow axis and the other one fast

---

<sup>1</sup> Hamamatsu X10468-02

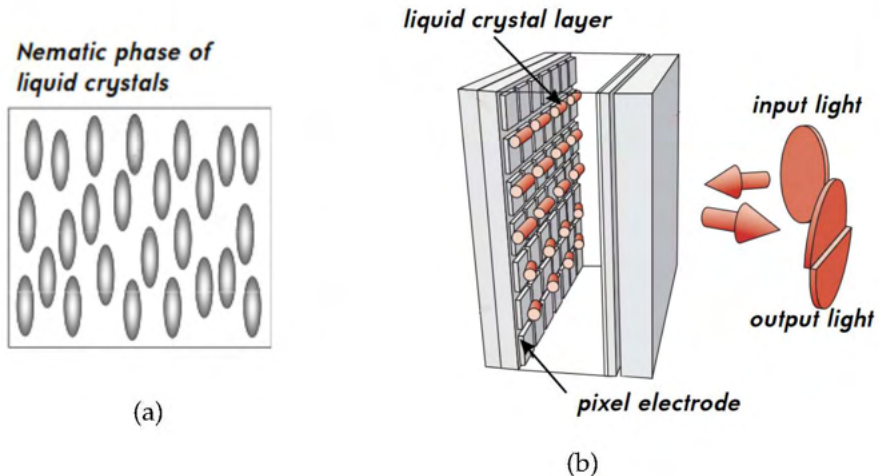


Figure 7: SLM basics. Figure a) shows the nematic phase of liquid crystals, where a long range parallel alignment prevails, adapted from [20]. Figure b) depicts the internal structure of a LCOS-SLM, where the molecules in the liquid crystal layer are locally controlled via pixel electrodes. Tilting the molecules results in the phase to be manipulated due to the birefringency of the molecules, adapted from [21].

axis. The propagation along these axes results in a phase difference. For a thorough treatment with Jones Matrices of how birefringence exactly affects the phase the reader is referred to [22] and Goodman [18].

The refractive indices experienced by the light can be changed by tilting the molecules locally in the nematic cells (the pixels of the SLM), resulting in the capacity of locally retarding the wave front by a specific phase difference.

In order to tilt the molecules the permanent electric dipole moment  $\mathbf{p}$  of the LC-molecules is used. An external electric  $\mathbf{E}$  field along a nematic cell will result in a torque  $\mathbf{M}$  acting on the molecules:

$$\mathbf{M} \propto \mathbf{p} \times \mathbf{E}. \quad (4)$$

Thus, the torque tilts the molecules in the direction of the electric field.

Addressing such nematic cells is realized by electrodes on a CMOS<sup>2</sup>-backpanel. To prevent permanent chemical change of the molecules, AC-voltage is applied.

For the phase modulation to take place the incident light needs to be linearly polarised in parallel to the untilted molecules. This is why

---

<sup>2</sup> complementary metal-oxide-semiconductor

in the final setup e.g. polarising beam splitters are a strict requirement.

It is worth mentioning that amplitude modulating LCOS-SLMs also exist. To that end the SLM locally changes the polarization of the light. Here a different nematic alignment in the cell is needed, the so called *twisted nematic phase*, where the molecules along the cell are gradually twisted by 90 degrees perpendicular to the light propagation. A polarisation analyser behind these cells results in a polarisation dependent attenuation for each pixel. Nevertheless the disadvantages of a really low efficiency, which leads to a pixelization of the created light fields, outweigh the advantage of being able to directly modulate the amplitude, such that phase-modulating SLMs are often the device of choice.

### 2.2.2 Hamamatsu SLM

The phase-only-modulating Spatial Light Modulator used throughout the work for this thesis is the X10468-02 LCOS-SLM manufactured by Hamamatsu. This model is optimized for a wavelength of 785nm and can handle power of up to 5W. Due to the properties of liquid crystals, extreme temperatures ( $< -10^{\circ}\text{C}$  and  $> 40^{\circ}\text{C}$ ) can have irreversible damaging effects and thus have to be avoided.

The liquid crystal chip has a size of 15.8mm  $\times$  12mm and consists of  $792 \times 600$  pixels. The fill rate of the pixels amounts to 98%, and incoming light is utilized to 97%. Thus the space in between pixels, where light can not be modulated, is relatively small. This unmodulated light is focused into a certain spot, known as the zero order spot, whose influence on desired targets has to be taken into account when using a SLM.

The pixels can individually modulate the phase by up to  $2.469\pi$ . The accessible phases are discretised by 256 (8 bit) input levels. The maximum phase shift is an important value to correctly control the SLM. The control is realized by converting the phase patterns into grey scale images with values ranging from 0 to 255. According to the manufacturer a grey scale value of 205 corresponds to a  $2\pi$  phase shift. This value is referred to as the  $2\pi$  value in the SLM-control-program as the generated phase patterns are calculated as modulo  $2\pi$ . Consequently the applicable phase levels are discretised by steps of size  $\frac{2\pi}{256} = 7,8125 \times 10^{-3}$ .

The SLM controller unit is connected to a computer via DVI-D, where the SLM is recognised as a second monitor, for which the resolution has to be set to  $800 \times 600$  pixels. Hence, all simulations have

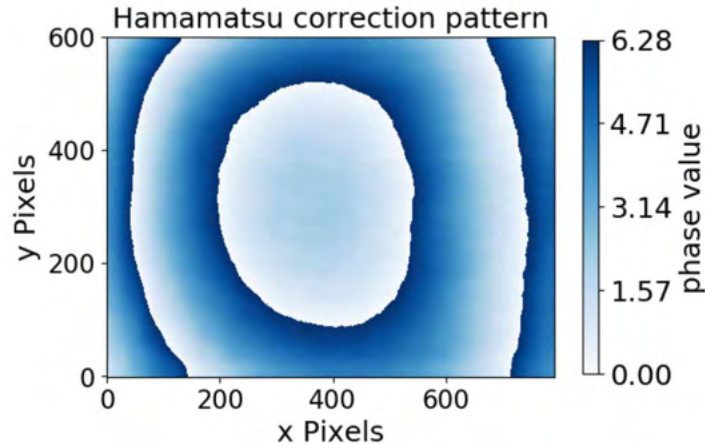


Figure 8: Correction phase pattern provided by the manufacturer in order to account for the non-uniform flatness of the surface of the SLM.

been also computed for an array of  $800 \times 600$  pixels. Adding a phase pattern consists of changing the background of the second monitor, a feature that is implemented in the used LabVIEW-program.

The updating process of the SLM-phase pattern is limited by a refresh-rate of 120Hz and the time needed for the liquid crystal molecules to adjust to the external electric field. For a phase shift from 10% to 90% of  $2\pi$  the rise time is 30ms and the fall time 80ms.

As the SLM-surface is not perfectly flat the manufacturer provides a unique correction pattern for our device (see figure 8) and recommends using it for any kind of desired target intensity. It has to be added to the calculated phase patterns for specific targets.

### 2.3 FOURIER OPTICS AND FRAUNHOFER DIFFRACTION

It has now become clear how we can manipulate the phase of light with an SLM, but how does that actually change the intensity of light in the far field? In order to understand, why the final relation between far field and SLM plane is simply a Fourier transform, it is worth to go through the underlying principles of Fraunhofer diffraction.

Our considerations start from the Huygens-principle, closely following the classical textbook on Fourier optics by Goodman [18]. The reader may wish to read this reference for deeper insights, e.g. about the preceding principles of scalar diffraction theory.

Huygens-principle states that each point of a wavefront can be regarded as a new source of a spherical wavelet. In return a planar wavefront can be regarded as the envelope or sum of many such wavelets.

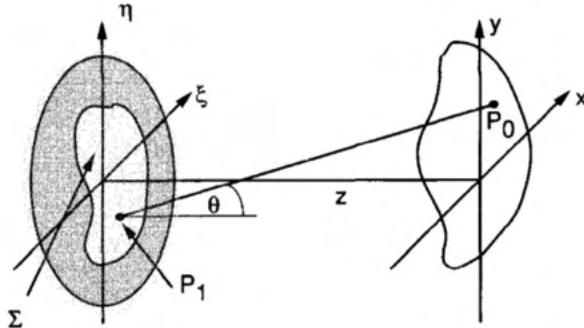


Figure 9: Diffraction through an arbitrary aperture  $\Sigma$ , from [18]

Since we are considering scalar diffraction, we assume monochromatic and scalar light fields with a wave number  $k$  in the following. The initial situation is depicted in figure 9. On the left hand side an aperture  $\Sigma$  lies in the diffraction plane. An elementary spherical wave with wave number  $k$  and wavelength  $\lambda$  propagating from  $P_1 = (\eta, \xi)$  in the diffraction plane has the form  $E \propto \frac{e^{ikr}}{r}$ , so that the field in a point  $P_0 = (x, y)$  of the image plane can be formulated by the *Fresnel-Kirchhoff-diffraction formula*:

$$E(x, y) = \frac{1}{i\lambda} \iint_{\Sigma} E(\xi, \eta) \frac{\exp(ikr)}{r} \cos \theta \, ds, \quad (5)$$

where  $ds$  denotes an integration along  $\Sigma$  and  $r$  is the length of the vector  $r$  from  $P_0$  to  $P_1$ ,

$$r = \sqrt{z^2 + (x - \xi)^2 + (y - \eta)^2} \quad (6)$$

and  $\theta$  is the angle between  $\mathbf{r}$  and the normal of the aperture plane. Equation 5 can be formulated in Cartesian coordinates using  $\cos \theta = \frac{z}{r}$ :

$$E(x, y) = \frac{z}{i\lambda} \iint_{\Sigma} E(\xi, \eta) \frac{\exp(ikr)}{r^2} d\xi d\eta. \quad (7)$$

Now the Fresnel-approximation is used to further reduce this integral. Assuming  $z$  to be large compared to the aperture and the image size one can use the Taylor expansion of a term of the form  $\sqrt{1+b}$  up to the first order

$$\sqrt{1+b} \approx 1 + \frac{1}{2}b \quad (8)$$

to rewrite  $r$  as

$$r = z \sqrt{1 + \underbrace{\left( \frac{x-\xi}{z} \right)^2 + \left( \frac{y-\eta}{z} \right)^2}_b} \approx z \left[ 1 + \frac{1}{2} \left( \frac{x-\xi}{z} \right)^2 + \frac{1}{2} \left( \frac{y-\eta}{z} \right)^2 \right], \quad (9)$$

When we introduce this approximated  $r$  in equation 7, we can further omit the second factor of  $r$  in the nominator. This cannot be done in the exponential function due to a large  $k$ .

$$E(x, y) = \frac{e^{ikz}}{i\lambda z} \iint_{\Sigma} E(\xi, \eta) \exp \left\{ i \frac{k}{2z} [(x-\xi)^2 + (y-\eta)^2] \right\} d\xi d\eta \quad (10)$$

Factoring out the terms independent of  $\xi$  and  $\eta$  and incorporating the limits of the aperture  $\Sigma$  into the field  $E(\xi, \eta)$  we are able to formulate the integral from  $-\infty$  to  $\infty$  as

$$E(x, y) = \frac{e^{ikz}}{i\lambda z} e^{i\frac{k}{2z}(x^2+y^2)} \iint_{-\infty}^{+\infty} [E(\xi, \eta) e^{i\frac{k}{2z}(\eta^2+\xi^2)}] e^{-i\frac{2\pi}{\lambda z}(x\xi+y\eta)} d\xi d\eta. \quad (11)$$

Here the Fourier transform of the complex field in brackets is recognisable. By introducing the strong far field Fraunhofer approximation, where we assume the propagation distance  $z$  to be significantly larger than the aperture size normalized to the wavelength, we obtain

$$z \gg \frac{k(\xi^2 + \eta^2)_{\max}}{2}. \quad (12)$$

Also neglecting the prefactors of equation 11 which are negligible for large  $z$ , equation 11 becomes

$$E(x, y) = \iint_{-\infty}^{+\infty} E(\xi, \eta) \exp \left[ -i \frac{2\pi}{\lambda z} (x\xi + y\eta) \right] d\xi d\eta. \quad (13)$$

If we introduce spatial frequencies

$$f_X = \frac{x}{\lambda z} \text{ and} \quad (14)$$

$$f_Y = \frac{y}{\lambda z}, \quad (15)$$

we finally obtain a simple Fourier transform relation between the fields in diffraction and image plane in the far field:

$$E(x, y) = \mathfrak{F}[E(\xi, \eta)] \left( \frac{x}{\lambda z}, \frac{y}{\lambda z} \right). \quad (16)$$

Thus, adding a phase  $\phi(\xi, \eta)$  to the complex field  $E(\xi, \eta)$  in the diffraction (SLM)-plane manifests itself through the Fourier transform of that input field, which will change both amplitude and phase of  $E(x, y)$  in the image plane.

It should be emphasized, that despite of phase and fields being the manipulated quantities, one is only able to measure the intensities  $I(x, y) = |E(x, y)|^2$  in the target and image plane. Our desired patterns will be initially stated as target intensities and not field distributions.

As the intensities define the energy of the beam, applying *Parseval's theorem* to our case:

$$\iint_{-\infty}^{+\infty} |E(\xi, \eta)|^2 d\xi d\eta = \iint_{-\infty}^{+\infty} |\mathfrak{F}[E(\xi, \eta)]|^2 dx dy = \iint_{-\infty}^{+\infty} |E(x, y)|^2 dx dy, \quad (17)$$

can be interpreted in terms of energy conservation. Hence, as one expects, no power is lost during the Fourier transform.

After all these approximations, we should realize how strong the approximations actually were. To calculate a concrete distance  $z$ , for which the Fraunhofer approximation (12) holds we can insert the size of our SLM-chip and the used wavelength of 780nm:

$$z \gg 400 \text{ meters} \quad (18)$$

This strong condition is obviously not feasible in a laboratory. The way to implement these strong conditions in practice is to use the interesting Fourier transforming properties of lenses. As lenses bundle parallel rays, that is, with the same wave vector (same spatial frequency), into a singular focal spot they actually perform a Fourier transform at the speed of light. In our setup the so 2f-setup is used, meaning that the lens is placed one focal length behind the SLM (the diffraction plane). The camera to observe the Fourier transform is positioned in the back focal plane of the lens (see figure 10). Hence, the Fourier relation of input and output field (equation 16) is evaluated for  $z = f$ . In the following  $z$  is always implicitly assumed to be the focal length.

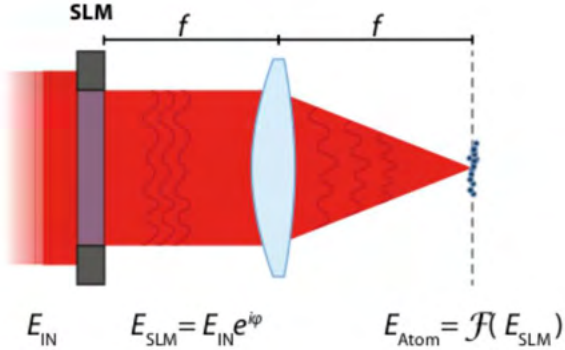


Figure 10: 2f SLM setup. In our case the input field is not passing through the SLM but reflected by it. The phase imprinted on the beam modulates both intensity and phase the Fourier plane, from [9].

### 2.3.1 Diffraction patterns of apertures

The SLM-chip represents a rectangular aperture, hence it is of interest to know which type of Fraunhofer diffraction pattern is to be expected when no additional phase is added to the incoming light field.

The amplitude transmittance of an rectangular aperture of size  $L_x \times L_y$  is given by

$$t_A = \text{rect}\left(\frac{\xi}{L_x}, \frac{\eta}{L_y}\right) = \begin{cases} 1 & \text{if } |\xi| \leq \frac{L_x}{2} \wedge |\eta| \leq \frac{L_y}{2} \\ 0 & \text{else} \end{cases}. \quad (19)$$

Fourier transforming this function results in an intensity pattern of

$$I(x, y) = L_x^2 \cdot L_y^2 \cdot \text{sinc}\left(\frac{L_x x}{\lambda f}\right)^2 \text{sinc}\left(\frac{L_y y}{\lambda f}\right)^2, \quad (20)$$

where  $\text{sinc}(x) = \sin(x)/x$ . Figure 11a shows the shape of a  $\text{sinc}(x)^2 \cdot \text{sinc}(y)^2$ -function and figure 11b the Fourier image of the SLM. After aberration correction the cross like shape is recognisable. The larger extent in vertical direction comes from the fact that the SLM has a shorter height  $L_y$  than width  $L_x$ , hence the spacing of the sinc-spots is larger vertically, though the spacing itself is not visible.

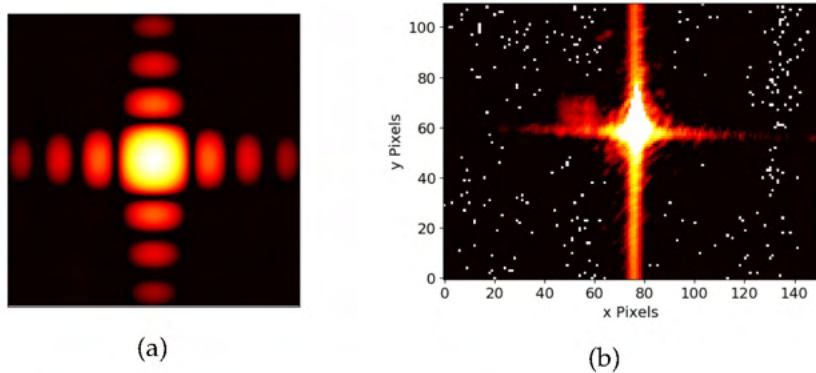


Figure 11:  $\text{sinc}(x)^2 \cdot \text{sinc}(y)^2$  plotted with logarithmic color scale (a) and Fourier image of the SLM (b).

Another prominent type of diffracting aperture is the circular aperture. Its amplitude transmittance can be stated as

$$t_A(r) = \text{circ}\left(\frac{r}{R}\right), \quad (21)$$

where  $R$  is the aperture radius and  $r = \sqrt{x^2 + y^2}$  the radius in the aperture plane.

Performing the Fourier transform results in an intensity distribution

$$I(r) = \pi^2 R^4 \left[ 2 \frac{J_1(kRr/z)}{kRr/z} \right]^2, \quad (22)$$

where  $J_1$  is a Bessel function of the first kind,

$$J_1(x) = \frac{1}{\pi} \int_0^{\pi} \cos(n\tau - x \sin \tau) d\tau. \quad (23)$$

This distribution is known as the Airy pattern, see figure 12a. The radius of the central intensity maximum is given by

$$d = 1.22 \cdot \frac{\lambda_f}{R}. \quad (24)$$

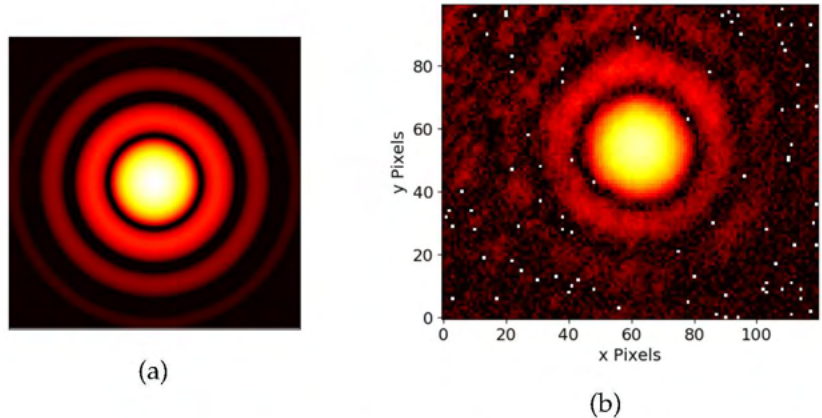


Figure 12:  $\left(\frac{J_1(r)}{r}\right)^2$  plotted with a logarithmic color scale (a) and airy diffraction like pattern created with the SLM.

During this thesis we will also draw back to this knowledge when using the SLM as a circular aperture (section 5.2). An Airy pattern created with the SLM is shown in figure 12b.

### 2.3.2 Further specifications for the SLM

The characteristic spacing of the sinc pattern of an rectangular aperture (equation 20) already hints toward a very important value, the diffraction limit, which is governed by the size of SLM,  $L_x \times L_y$ :

$$\Delta x \times \Delta y = \frac{\lambda f}{L_x} \times \frac{\lambda f}{L_y}. \quad (25)$$

Applying  $f = 150\text{mm}$ ,  $L_x = 15.8\text{mm}$ ,  $L_y = 12\text{mm}$  and  $\lambda = 780\text{nm}$  we obtain

$$\Delta x = 7.405 \mu\text{m} \text{ and} \quad (26)$$

$$\Delta y = 9.750 \mu\text{m}. \quad (27)$$

If the SLM is completely illuminated (assumed equivalent to a sufficient Gaussian beam width), the smallest feature we can create on purpose in the image plane should be exactly at the diffraction limit. With an improved objective in the final experiment this limit could be pushed to a few  $\mu\text{m}$  where the Rydberg blockade radius lies. Throughout this thesis  $\Delta x$  and  $\Delta y$  are denoted as one focal unit (f.u.). It should be stressed that the focal unit is affected only by the total size of the SLM and not by the number of pixels  $N_x$  and  $N_y$  of the SLM. The latter influences how large the area we can control in the image plane is.

We should take into account that for our simulations and computations of phase patterns we are going to use Discrete Fourier transforms (DFTs). At first sight this seems unproblematic, as we can simulate the SLM's phase influence on a 2D array of  $792 \times 600$  pixels and

thus can Fourier transform into an array of the same size. But is this a realistic assumption for simulating the behaviour of the SLM setup?

If we assume the pixel size to be much smaller than the total area of the SLM these pixels  $(k, l)$  with a centre coordinate  $\xi_k, \eta_l$  and phase  $\phi_{kl}$  can be regarded as  $\delta$ -functions. Hence, the light field in the SLM  $E(\xi, \eta)$  plane is a Dirac comb like function depending on the input field  $E_i(\xi_k, \eta_l)$ :

$$E(\xi, \eta) \approx \sum_{k=0}^{N_x-1} \sum_{l=0}^{N_y-1} \delta(x - x_k) \delta(y - y_l) E_i(\xi_k, \eta_l) e^{i\phi_{kl}}. \quad (28)$$

Applying the continuous Fourier transform of equation 16 to the field  $E(\xi, \eta)$  results in the light field in the image plane to also be a  $N_x \times N_y$  grid of focal spots with the total size  $(N_x \cdot \Delta x) \times (N_y \cdot \Delta y)$ , such that we can discretise the image in points  $(m\Delta x, n\Delta y)$ :

$$E(m\Delta x, n\Delta y) = \sum_{k=0}^{N_x-1} \sum_{l=0}^{N_y-1} E_i(x_k, y_l) e^{i\phi_{kl}} e^{-i2\pi(km/N_x + ln/N_y)}. \quad (29)$$

For this reason the relation between both lights field can be realistically simulated using DFTs.

As a last remark in this section it is noted, that the created patterns are repeated periodically due to the last factor of equation 29, which is in practice limited by the size of the Fourier lens.

### 2.3.3 Basic phase operation

Someone who starts to get acquainted with Fourier transforms and Fourier optics will in general also start to build an intuition about frequency space, but application of this intuition is limited with a phase-modulating SLM: As we are only able to manipulate the phase and not the amplitude of light the central equation for this thesis can be simply stated as follows:

$$I_o(x, y) = |E_o(x, y)|^2 \stackrel{!}{=} |\mathcal{F}[\sqrt{I_i(\xi, \eta)} e^{i\phi(\xi, \eta)}]|^2. \quad (30)$$

Where  $I_o$  is the desired intensity and  $I_i$  the input intensity imposed by the gaussian laser beam.  $\phi(\xi, \eta)$  is the phase distribution in the SLM-plane that needs to be found. In most cases the solution will not even be unique. A simple Fourier backtransform is not rewarding because of the  $I_i$  constraint. Solving this problem and finding a suited Fourier transform pair is the subject of chapter 3 and 4, nevertheless there are few simple phase distributions that create characteristic Fourier images. Three of them are presented in the following and should be kept in mind.

## LINEAR PHASE GRADIENTS

A basic theorem about Fourier transforms which follows straight forward from the definition is the *Shift theorem*.

Assuming a DFT for a vector  $\mathbf{x}$  represented by  $[x_n]$ :

$$\mathfrak{F}\{[x_n]\}_k = X_k, \quad (31)$$

then adding a linear phase  $e^{\frac{i2\pi}{N}mn}$  for some integer  $m$  results in replacing  $X_k$  by  $X_{k-m}$ :

$$\mathfrak{F}\{[x_n \cdot e^{\frac{i2\pi}{N}mn}]\}_k = X_{k-m}. \quad (32)$$

This means that a linear phase shift in the spatial domain introduces a shift in the frequency domain and vice versa. This property can be used to shift the target intensities by imposing a linear gradient of phase in the SLM-plane  $e^{i\Phi_{grad}} = e^{i(ax+by)}$ . Applied to the DFT simulations with  $792 \times 600$  arrays and taking into account that the phase is displayed on the SLM as a grey scale value ranging from 0 to 255, the phase gradient needed to shift a specific pattern by one focal unit is:

$$a = 2\pi \cdot \frac{256}{792} = 2.029 \text{ in } x\text{-direction and} \quad (33)$$

$$b = 2\pi \cdot \frac{256}{600} = 2.680 \text{ in } y\text{-direction.} \quad (34)$$

As we have to take the modulo of 255 due to the phase modulating limit this linear phase gradient effectively results in a blazed grating, but we should note that with this simple linear phase gradient definition the modulation depth is always set to  $2\pi$  when the greyscale value 255 is reached. In this sense the maximum spot shift is created by a blazed grating consisting of three phase levels with a step size of  $128 \equiv \pi$ . Hence, the maximum shift amounts to  $\frac{128 \cdot 2\pi}{a} = 396$  focal units in  $x$ -direction and  $\frac{128 \cdot 2\pi}{b} = 300$  focal units in  $y$ -direction. If one specifically wants to reproduce blazed gratings with an SLM a variable modulation depth should be included into the linear phase gradient definition.

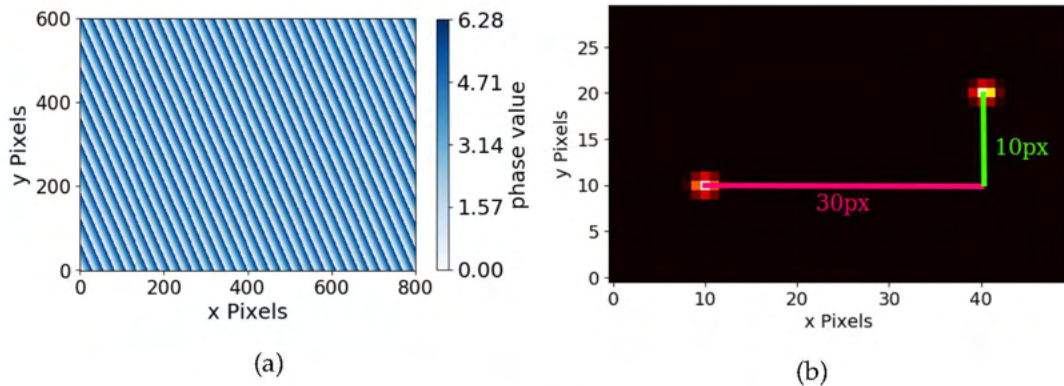


Figure 13: Application of the Shift theorem. A linear phase gradient 30a and 10b (a) results into a spot shift in the Fourier plane (b) (simulation)

CONICAL GRADIENTS

For a linear gradient in radial direction of the form

$$K = a \cdot r = a \cdot \sqrt{x^2 + y^2}, \quad (35)$$

where  $a$  is the applied conical gradient constant, the resulting effect is similar to the linear phase gradient. Using the Fourier transform in polar coordinates one can show that this kind of linear gradient (see figure 14a) similarly leads to a spot shift. However, due to the radial shifting a ring-like structure is created (see figure 14b). Note that due to the non-quadratic size of our SLM-pixel arrays the rings are in fact slightly elliptic. To create perfect rings we can use the factors  $a$  and  $b$  from the previous section on linear phase gradients.

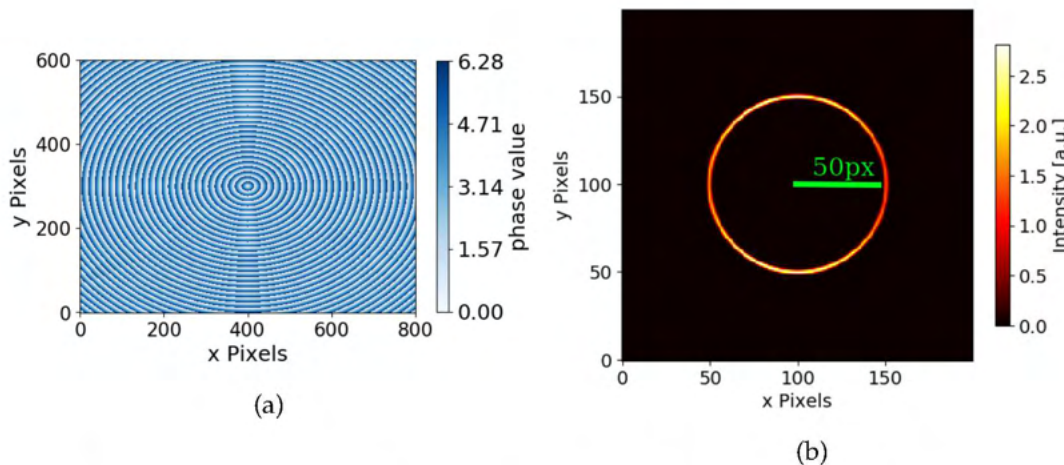


Figure 14: Effect of a radial linear gradient. A conical linear phase gradient of  $\alpha = 50$  (a) yields a ring pattern with radius 50 pixels (b).

## QUADRATIC PHASE PATTERNS OF LENSES

Lenses can be described in terms of a thickness functions. A thin lens with focal length  $f$  effectively adds a quadratic phase pattern to the light field [18]

$$\phi(x, y) = \frac{1}{f}(ax^2 + by^2). \quad (36)$$

To enable further tweaking it is convenient to implement stretching factors  $a$  and  $b$  in both directions. Thus, such quadratic phase patterns can be used with an SLM to reproduce the effect of lenses. In the simulations the quadratic phase patterns with different  $f$  can be used to enlarge the intensity patterns (see figure 15a). Again the effect of having to take the phase modulo comes into play. If a large prefactor is chosen the cross section of the phase patterns resembles the one of a Fresnel-lens.

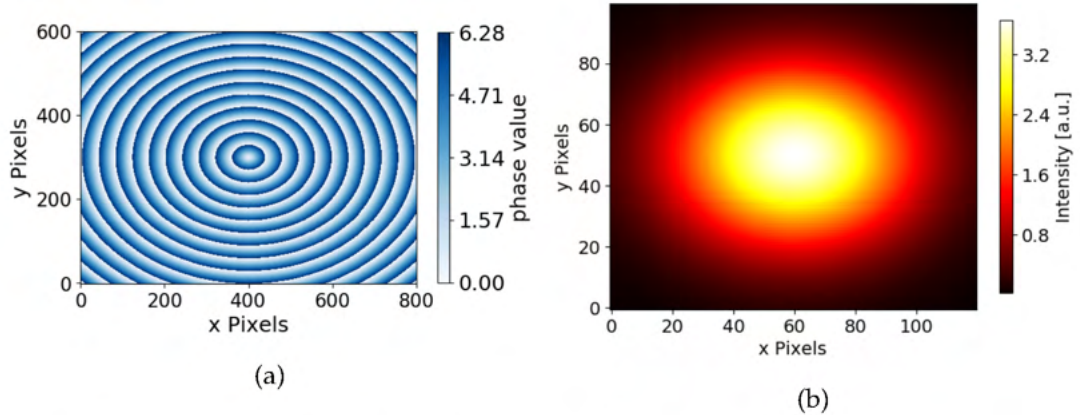


Figure 15: Effect of a quadratic phase gradient. This type of phase pattern (a) results into a widening of the spot in the image plane (b).

# 3

## GENERATION OF PHASE PATTERNS

---

The central question, that has to be treated, is:

How can we achieve specific intensity distributions by phase-modulating a laser beam only, the desired target intensity and the Gaussian input amplitude being the given constraints? Due to these constraints that are imposed by the use of a phase modulating spatial light modulator, the approach of simply performing one Fourier transform is not working.

Solutions to this kind of mathematical problem are phase retrieval methods. To gain a better understanding where the considerations for phase retrieval algorithms originate from a short digression on holography is made. After that the iterative Fourier transform algorithm as a solution to that problem is presented. In addition the possibility of calculating the phase patterns analytically is discussed.

### 3.1 HOLOGRAPHY

Holography is a fascinating technique that has gained large attention since its first proposition by Gabor in 1948 [5]. The general idea of holography is to record amplitude and phase of an optical wave scattered by a coherently illuminated object, such that these properties can later be reconstructed. The recording is done by means of interferometry, that is, the interference pattern of a reference wave and an object wave is recorded, for instance with a photographic plate (see figure 16). If this recording medium is transparent and illuminated with a properly chosen reconstruction beam, the original object wave front can be restored, meaning that an image of the original object appears, without the object being physically present. For a mathematical description and thorough introduction to the different types of holography see *Goodman* [18]. With the advent of the laser, a highly coherent and monochromatic light source, in the 1960s holography could be continuously improved and investigated.

Initially, holography was a purely experimental problem, but soon the question arose, whether it would also be possible to simulate holography with computers, which lead to emergence of the field of study of computer-generated holography (CGH). These simulations are not directly linked to physically creating holograms, but they allow for substituting elaborated interference measurements, such that one can also create images of objects that never had to be physically

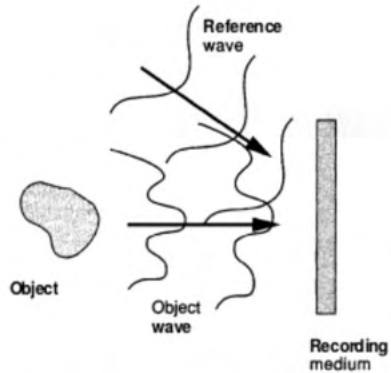


Figure 16: Original hologram recording principle. The interference pattern of a reference wave and the wave of a coherently illuminated object contains the information that is necessary to reconstruct an image of the object by illuminating the recording medium with the reference wave, from [18]

existent. For Fourier-optical simulations the assumption was established, that most of the information is stored in the phase, yielding the concept of *kinoforms*, the phase patterns imprinted on an input field in order to generate some kind of desired target field distribution.

Consequently a lot of knowledge and several methods for *phase retrieval* have been produced. The connection of holography and a phase modulating Spatial Light Modulator lies in the fact that we can use the device as a reconfigurable recording medium in order to encode information on a laser beam. Hence, the knowledge of computer-generated holography is of great use for calculating the necessary phase patterns.

### 3.2 ITERATIVE FOURIER TRANSFORM ALGORITHMS

A breakthrough in numerically solving the phase retrieval problem in Computer-generated holography was achieved by Gerchberg and Saxton in 1972 [23]. Iterative Fourier transform algorithms, short IF-TAs, that have since then been intensely studied, are also referred to as Gerchberg-Saxton-Algorithms. The basic idea is to iteratively fourier-transform back and forth between the image plane (the desired target distribution) and the diffraction plane (the SLM-plane in our case) and to apply the given intensities as constraints each time until convergence.

More precisely one iteration of the algorithm consists of four stages, visualized in figure 17. The algorithm "relies on the fact that a change in the amplitude distribution alone in one domain of the Fourier

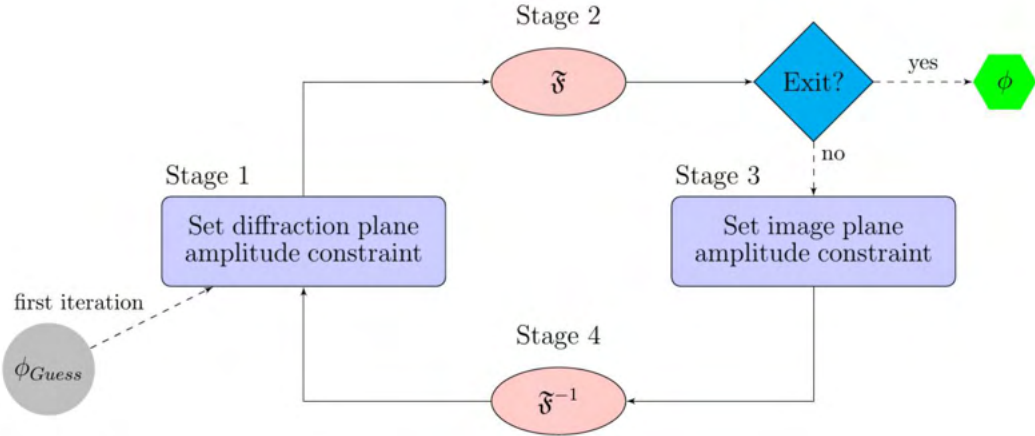


Figure 17: Iterative Fourier transform algorithm scheme

transform will result in changing both the amplitude and phase distribution in the opposite domain"[23].

#### THE FOUR STAGES OF THE IFTA

1. In the first iteration the constraint amplitude  $\sqrt{I_{SLM}(x, y)}$  in the diffraction (SLM)-plane is combined to a complex field with an initial phase  $\phi_0$ :

$$A_{SLM}(x, y) := \sqrt{I_{SLM}(x, y)} \cdot e^{i\phi_0(x, y)} \quad (37)$$

In the following iterations the amplitude constraint is also applied, but the phase resulting from the precedent step 4 is kept.

2. This complex distribution is Fourier-transformed into the image plane

$$\mathcal{F}[A(x, y)] = A_t(x, y) \cdot e^{i\phi_t(x, y)} \quad (38)$$

3. The resulting amplitude  $A_t$  is replaced by the target constraint amplitude  $\sqrt{I_t(x, y)}$ , the phase  $\phi_t$  is kept.

$$A_t(x, y) \cdot e^{i\phi_t(x, y)} \rightarrow \sqrt{I_t(x, y)} \cdot e^{i\phi_t(x, y)} \quad (39)$$

4. The distribution is then transformed back into the diffraction plane with an inverse Fourier-transform

$$\sqrt{I_t(x, y)} \cdot e^{i\phi_t(x, y)} \rightarrow \mathcal{F}^{-1}[\sqrt{I_t(x, y)} \cdot e^{i\phi_t(x, y)}] \quad (40)$$

When a fixed termination condition, like the minimisation of an error, is reached the algorithm stops and outputs the phase pattern  $\phi_{SLM}(x, y)$  (obtained in stage 4) and the simulated target intensity

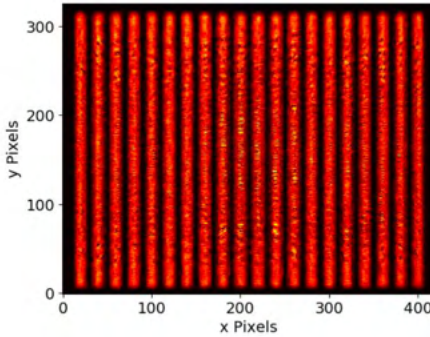


Figure 18:  $\sin(x)^2$  target simulated with the classical IFTA. The algorithm is not able to correct the imperfections with ongoing iterations.

$A_t(x, y)^2$  as the values of interest.

It is not obvious that this iterative approach is converging, but the authors showed that this is in fact an error reducing algorithm (an error definition is introduced in chapter 4), reaching convergence of the error into a local minimum with ongoing iterations. Proving the convergence has been subject of a more rigorous mathematical treatment by Fienup [24].

As target and diffraction amplitude are discretised, Discrete Fourier-transform (DFT) computations for an array of  $N_x \times N_y$  pixels are needed. They are calculated using Fast Fourier-transforms (FFTs), significantly reducing the complexity of the algorithm from  $\mathcal{O}(N^2)$  to the optimal complexity of  $\mathcal{O}(N \log_2(N))$ , where  $N = N_x \cdot N_y$ . Due to the Nyquist-Shannon-sampling theorem, it is necessary to embed the target in an array of at least twice the original size (increasing the calculation time) for the full resolution to be reached by the Fourier transforms, for more details see [10].

The classical IFTA can be used efficiently for discrete targets like spot arrays [8, 10], but will not produce good results for continuous targets as has been widely reported. As a demonstration of that fact a sinusoidal pattern was computed (see figure 18). The general inhomogeneity is persisting with further iterations. As the desired intensity patterns are of continuous form, we will thoroughly go through a slightly modified version of an IFTA in the next chapter. It includes some additional amplitude degree of freedom, that facilitates the task for the algorithm to find an accurate solution.

### 3.3 ANALYTIC BEAM SHAPING

In addition to the numerical solutions, from early on analytic solutions for the phase retrieval problem have been investigated, which

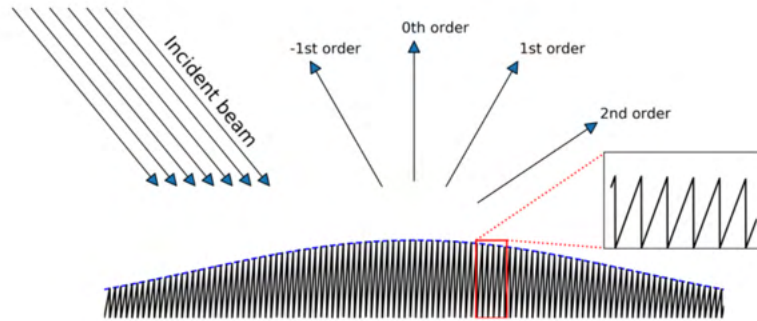


Figure 19: Blazed grating method, where the grating depth decides on how much of the light is locally diffracted into the first order. This allows for also modulating the amplitude in the SLM plane, from [28].

are also referred to as geometrical beam shaping.

One possible analytical solution consists of finding a coordinate transform between diffraction and image plane as introduced by *Aagedahl et al.* [25]. This method requires that the intensities distributions have a separable form, meaning that  $I(x, y) = I_X(x) \cdot I_Y(y)$  (like for a Gaussian distribution), such that for each dimension the appropriate coordinate transform can be found. That kind of beam shaping has not been practically tested for this thesis, although target intensities of the form  $\sin x^2 \cdot \text{rect}(y)$  are separable and therefore suited for this kind of method. The disadvantage is that this method requires invertible continuous functions. As the target intensity distributions are discretised they would need to be inverted with numerical tools, which may introduce additional errors. In spite of this inconvenience, the method has been reported to be successful, both in simulations and experiment [8, 26].

Other analytical solutions do not require for the intensity distributions to be separable. A recent paper by *Clark et al.* [27] reviews a variety of analytic phase retrieval methods that are also applied to beam shaping. They all work on the principle of modeling phase distributions as blazed gratings, such that light is controlled into one specific order. The crucial point is that locally varying the "depth" of the grating also effectively allows for a precise amplitude control in the diffraction plane, which can also be applied to a SLMs (19). This profound insight has also been investigated closely by *Hammel* [28]. The main advantage of analytic beam shaping algorithms is that, they will in principle just require carrying out one singular Fourier transform. This allows for setting the phase as a constraint in the target plane in addition to the intensity, a possibility that was omitted

with iterative Fourier transforms.

In this section an excerpt of solutions for the phase retrieval problem were presented. Although we are going to proceed with an adaptation of the Iterative Fourier-transform algorithm in the next section, the possibility of analytical phase retrieval and thus beam shaping was outlined because of its possible use for subsequent work as discussed in chapter 6.

It should be stressed that solutions to the phase retrieval problem are in general not unique. This is due to the fact that only the amplitude and not the phase is a constraint in the target plane. Furthermore beam shaping is by far not the only field of application of this initially purely mathematical problem, for an overview see [29].

# 4

## THE MRAF-ALGORITHM

---

A modern version of an Iterative Fourier transform for phase retrieval problems is the Mixed-Region-Amplitude-Freedom algorithm, in short MRAF, that was proposed in 2008 by Pasienski and DeMarco [26, 30]. They designed it specifically for the purpose of experiments with ultracold atoms and it offers a great versatility for all kinds of desired targets in combination with small simulation errors. This chapter explores the subtleties of implementing an iterative Fourier transform algorithm with an emphasis on the MRAF. After these computational considerations we will then finally be able to test the generated phase patterns in our SLM setup.

### 4.1 THE GENERAL IDEA

The MRAF-algorithm enhances the Gerchberg-Saxton-algorithm by segmenting the target plane into two regions, a signal region SR and a noise region NR, in the latter total amplitude freedom is allowed, hence the name. The target intensity constraint is only applied in the signal region. A mixing parameter  $m$  defines how the light is relatively distributed between these two regions. Subsequently, the third IFTA stage (equation 39) is replaced by:

$$A_t(x, y) \cdot e^{i\phi_t(x, y)} \rightarrow \\ (m \cdot \sqrt{I_t(x, y)}|_{SR} + (1 - m) \cdot A_t(x, y)|_{NR}) \cdot e^{i\phi_t(x, y)}. \quad (41)$$

In the simulations mixing parameters between 0.3 and 0.5 have been proven to be valuable with regard to the figures of merit that are depicted in the next section. Not defining a noise region and setting  $m = 1$  is equivalent to the classical IFTA.

Typical noise masks have a circular or rectangular shape (see figure 20). In general the influence of the distance between target and noise region seems to be negligible, a noise mask tight to the target pattern does not necessarily produce better simulations. However, the specific form and size of the noise mask may be of interest with regard to the geometry of the atoms in the final experiment, more sophisticated noise masks are in principle also conceivable [30].

In fact the concept of allowing some amplitude freedom has been discussed before (as briefly mentioned in the MRAF-paper), the only difference being that the mixing factor was not fixed, see for instance *Akahiro* in 1986 [31].

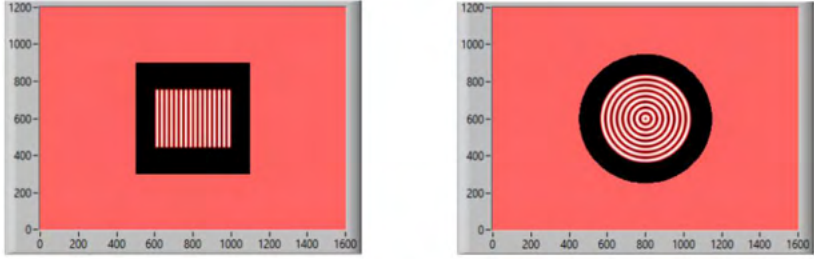


Figure 20: Noise regions around specific targets. The large canvas size is due to the Shannon-Nyquist sampling theorem, all calculations are done one arrays with twice the actual size.

#### 4.2 FIGURES OF MERIT

Quantifying the quality of the simulations is an essential task as one has to be able to judge if the accuracy of the targets is high enough for the implementation of the phase pattern in the final experiment.

Several figures of merit can be defined. First, one may be interested in the efficiency of the MRAF-Algorithm if the available laser power is of concern. The efficiency  $\xi$  is defined as the portion of light intensity  $I(x, y)$  distributed into the signal-region relative to the total light in the signal and noise region:

$$\xi = \frac{\sum_{x, y \in SR} I(x, y)}{\sum_{x, y \in SR \cup NR} I(x, y)} \quad (42)$$

It seems quite obvious that the efficiency is somehow correlated to the mixing parameter. Although, the efficiency is not equal to the mixing parameter, the efficiency always depends on the specific target and noise mask. Typical values are 16% for  $m=0.3$ , 44% for  $m=0.5$  and 80% for  $m=0.6$ , which are the mixing parameters which yield the best results.

Most importantly, a Root-mean-square-error (RMSE) has to be defined. I followed the suggestion made by the authors of MRAF[30], calculating the squared deviance of simulation and target only for pixels where the target is non-zero. This region is called the measure region (MR) which consists of  $N_{MR}$  pixels.

$$RMSE = \sqrt{\frac{1}{N_{MR}} \sum_{x, y \in MR} \frac{(\tilde{I}_{sim}(x, y) - \tilde{I}_{targ}(x, y))^2}{\tilde{I}_{targ}(x, y)^2}} \quad (43)$$

For simulation and target intensities to be comparable both have to be normalized to the same power in the measure region, such that

$$\tilde{I}(x, y) = \frac{I(x, y)}{\sum_{x, y \in MR} I(x, y)} \quad (44)$$

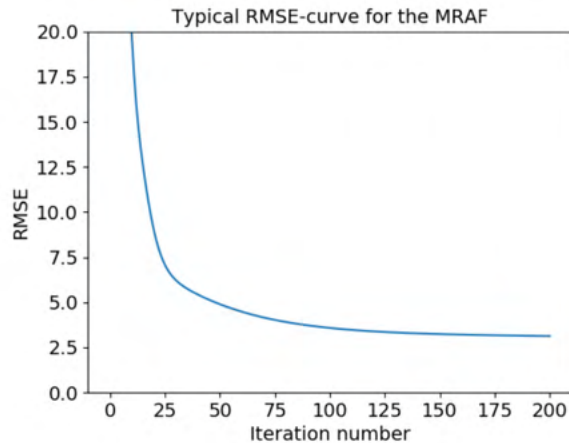


Figure 21: Evolution of the RMSE for a  $\sin^2$ -target. The MRAF will in general come to near stagnation after at least 200 iterations (first RMSE values  $>20\%$ )

Figure 21 shows a typical RMSE evolution curve for the MRAF algorithm. After drastic improvements throughout the first iterations, the algorithm converges quickly. From the 100<sub>th</sub> to the 200<sub>th</sub> iterations only small improvements are reached as the algorithm almost reached its minimum RMSE of  $\sim 3\%$ . 200 iterations typically take 2 minutes of computation time.

The simulations are realized in a LabVIEW-environment. For the program to finish two break conditions are used: A certain minimal change of the RMSE from one iteration to the next and setting a maximum number of iterations as a limit.

Interestingly, the introduction of the amplitude freedom in combination with our error-definition contradicts the original notion of the IFTA as a monotonic error-reducing algorithm [23, 24]. Situations can be simulated in which the RMSE will rise again from one iteration to next. Nevertheless, this phenomenon could only be observed during the first iterations of the algorithm.

Another simple figure of merit is a deviation map of the target and the according histogram, that can contribute to an informed judgment about the quality and homogeneity of the simulations. The  $\sin^2$ -targets offer the advantage that one can also go into frequency space and observe how distinct the two expected peaks appear. This figure of merit can be relevant in the experimental setup where other error metrics can not easily be applied.

### 4.3 THE INITIAL PHASE GUESS

Up to now we did not pay much attention to the initial guess that is assigned to the diffraction amplitude in stage one of the first iteration of an IFTA (equation 38).

It is important to realize that once the initial guess is set the algorithm is deterministic. It predetermines towards which RMSE the algorithm will converge (but that we do not know in advance).

#### 4.3.1 Creation of optical vortices by phase singularities

The RMSE alone gives not all the information about the quality of the fit. Unwanted speckles, meaning dark spots of zero intensity, will appear in the simulated target depending on the initial phase guess. Most of these speckles will not be removed even with further iterations of the algorithm, causing the RMSE to stagnate at a high value. Figure 22 shows such speckles for some arbitrary patterns, in figure 22a a constant initial phase guess of zero was chosen, in figure 22b a randomized phase pattern was used.

The emergence of such speckles can be traced back to *optical vortices*, which have a connection to the subject of angular orbital momentum of light [32]. With optical vortices Laguerre-Gaussian-modes of a beam can be created [28].

Ever since IFAs have been used for continuous 2D images the emergence of speckles has been intensively investigated [25, 33, 34]. Speckles can occur due to spiral phase singularities. At such an isolated singularity lines of constant phase intersect, such that the phase

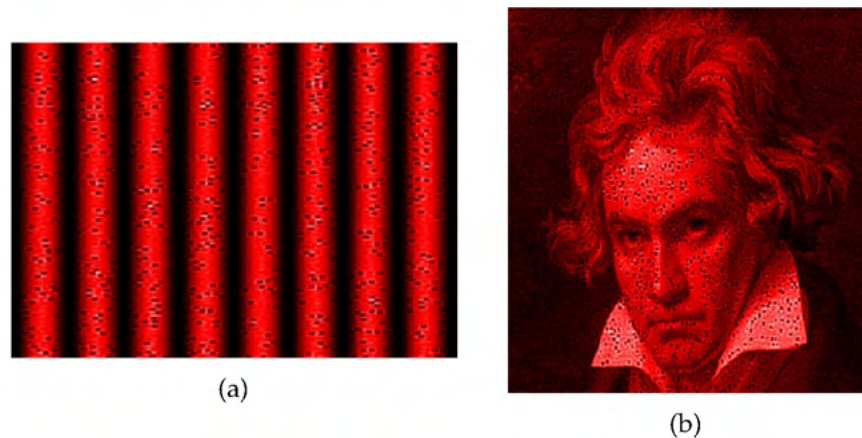


Figure 22: Speckled  $\sin^2$  and Ludwig van Beethoven created by not choosing a suitable initial phase

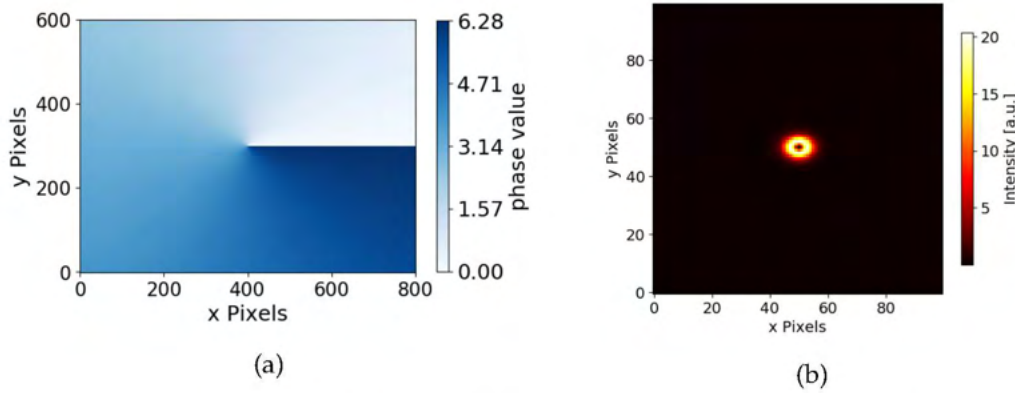


Figure 23: Phase singularity of order  $m=1$  (a) and simulated creation of a vortex in a gaussian beam (b)

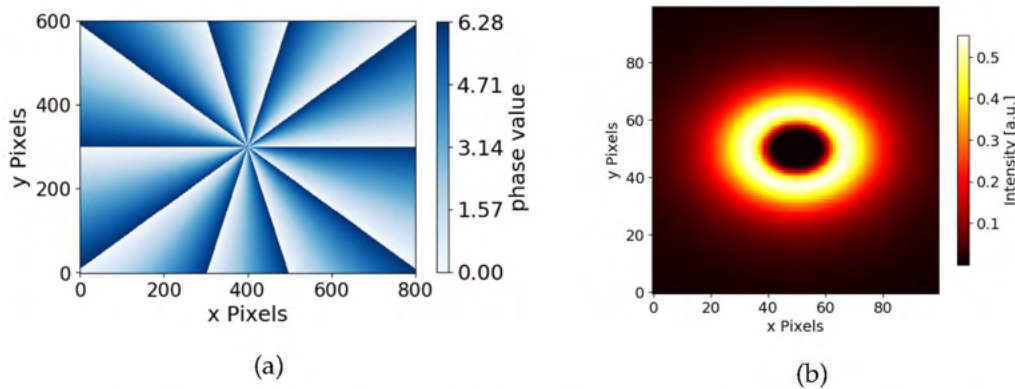


Figure 24: Phase singularity of order  $m=10$  (a) and simulated creation of a vortex in a gaussian beam (b)

assumes all values between  $0$  and  $2\pi$ . The phase-distribution around such a singularity at position  $(x_0, y_0)$  can be described as

$$\phi(x, y) = \arctan\left(\frac{y - y_0}{x - x_0}\right) \quad (45)$$

as illustrated in figure 23a. Irrespective of the traverse direction through a vortex core, a phase jump of  $\pi$  is observed. The light field thus contains a singularity at position  $(x_0, y_0)$  where the amplitude  $A(x_0, y_0)$  vanishes:

$$A(x, y)e^{i\phi(x, y)} = ((x - x_0) + i(y - y_0)) \cdot A_0, \quad (46)$$

here  $A_0$  is a constant. It is important to stress that the phase singularity has a direct effect on the beam, such that the vortex is already created in the SLM plane and not in the far field by the Fourier transform. The latter does not affect the vortex, such that in the Fourier-plane we also get a ring-like structure with a point of zero intensity in the centre.

Optical vortices are also produced by phase singularities of higher order, growing larger and larger (see figure 24b). The specific winding number  $m$  is called the topological charge of the vortex and is defined by the line integral along the optical vortex

$$m = \frac{1}{2\pi} \oint \nabla\phi(x, y) \cdot dl. \quad (47)$$

The topological charge is an integer, the counterpart of opposite sign of a phase singularity just being the counterrotated version. Canceling such a singularity consists of adding spiral phase singularities of opposite charge on each other.

The work in the references [34, 35] depicts that phase singularities introduced during the IFTA-procedure always appear as pairs of opposite charge with most phase singularities being of the first order ( $\pm 1$ ). In the first iterations of an IFTA self-annihilation of vortices can occur by accident if singularities of opposite charge are in each others vicinity. Nevertheless, this process of attracting, colliding and annihilating only functions over small distances, consequently the most vortices remain untouched.

#### 4.3.2 *Avoiding speckles*

As has been proofed mathematically in the references mentioned above, further iterations are unable to remove the speckles. Thus, some enhanced vortex elimination techniques have been proposed. They consist of automated phase singularity detection and artificially introducing singularities of inverse charge. More convenient would be the implementation of a softening factor  $\beta$  which gradually increases from 0 to 1 during the IFTA such that in stage 1 (equation 38) of the IFTA the phase of the previous  $n_{th}$ -iteration is kept in part,

$$\phi_{t n+1} = \beta \phi_{new} + (1 - \beta) \phi_n, \quad (48)$$

where  $\phi_{new}$  is the phase resulting from the preceding stage 4 and  $\phi_n$  the phase resulting from stage 4 of the second last iteration. That way, strong phase fluctuations introducing phase jumps of  $\pi$  and thus speckles should be avoided [8, 35].

The easiest method that proves to be entirely sufficient for our purposes and that I have used during my work is to not let the algorithm introduce speckles in the first place, and simply consists of choosing an appropriate initial phase guess.

To that end the knowledge about basic phase operations in Fourier transforms as presented in section 2.3.3 comes into play. The idea

is that with a good initial phase guess the first Fourier transform roughly matches the desired pattern. If this is the case the algorithm does not introduce drastic phase fluctuations that produce speckles.

A quadratic lens pattern can be used to make the prediction of the propagated input field roughly match the size of the target, for rectangular structures the stretching factors both in x and y direction are of use. If the target is not centered the prediction can be shifted to the right position with linear phase gradients. For targets with circular symmetry the conical gradient, that leads to a ring-target, can be used.

In general combinations of these three operations produce a good initial guess for a large range of desired target intensities, thus that the creation of vortices can be largely suppressed, as presented with the simulation demonstration in section 4.6.

Notice that another kind of vortices that is not predicted in the simulations, but that may occur in the experimental setup can be relevant. In consequence of the discretised nature of the SLM we are actually only able to control a grid of spots of the light in the focal plane, the amplitude in between resulting from interpolation. If two adjacent spots have a phase shift differing by  $\pi$  the amplitude in between vanishes or is at least attenuated, an effect illustrated in figure 25. The light field in between focal spots is not considered in our simulations, that is the reason why the simulations are not able to predict speckles created like this.

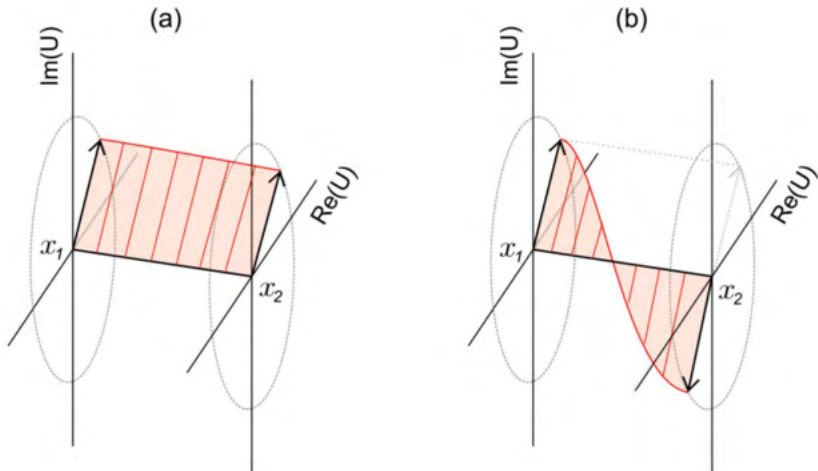


Figure 25: Illustration of amplitude vanishing due to a  $\pi$  phase jump between adjacent pixels/light spots. A phase jump of  $\pi$  implicates that the vectors of the complex field are diametrically opposed. Hence, the amplitude in between the spots vanishes, from [8].

#### 4.4 THE INPUT AMPLITUDE

It should also be stressed that taking the correct input amplitude for the calculations is obviously a condition for the simulations to be reproducible in the experiment. Therefore the correct width and the actual peak position of the Gaussian input amplitude have to be known. The effect of deviating values has not been studied in detail, but the deteriorating effects can be easily outlined by simulations for demonstration purposes.

It seems like an incorrect position and width guess of the beam does not drastically change shape of the targets, but primarily affects the homogeneity of their illumination as depicted in figure 26. Nonetheless also vortices can be introduced, see figure 26a. Hence a correct alignment and specification of the input beam on the SLM is not to be underestimated. In section 5.3 a method to measure the beam specification values directly with the SLM is presented.

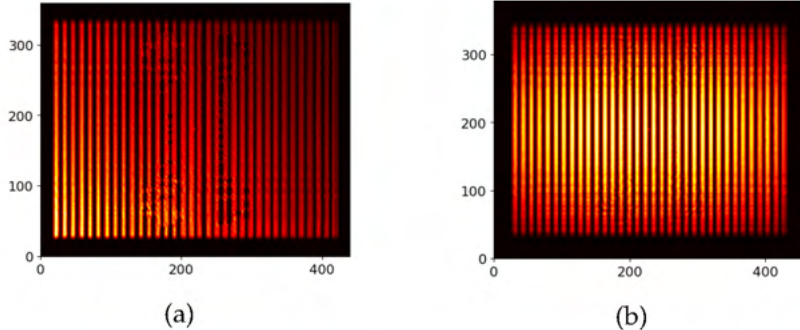


Figure 26: Effects of a wrongly guessed input amplitude. Our reference was set to (390, 300) pixels centre position and a beam width of 263 pixels. In a) the phase pattern for a  $\sin^2$  was propagated with a Gaussian beam at position (300, 250) and the correct width and in b) with a beam width of 180 pixels and the correct position. The sinusoidal shape is deteriorated especially with regard to the homogeneity of the illumination.

#### 4.5 REDUCTION TO A ONE-DIMENSIONAL PROBLEM

As is going to be presented in the next section, the MRAF-Algorithm is able to create simulations with a high accuracy. Nevertheless, it is worth considering that the computations on a two-dimensional array can be reduced to a one-dimensional task for specific targets. As both the desired intensity distributions of sinusoidal form and the assumed Gaussian input on the SLM are of separable form, more precisely  $I_{\text{input}} \propto e^{-r^2} = e^{-x^2} \cdot e^{-y^2}$  and  $I_t(x, y) = \sin(x)^2 \cdot \text{rect}(y)$ , it is conceivable to compute a phase distribution for each dimension separately. The separability principle is also exemplified in figure

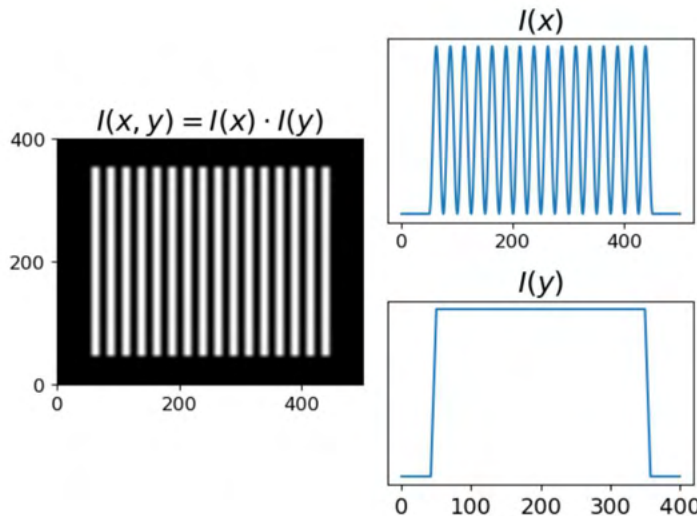


Figure 27: Concept of reducing a separable 2D intensity distribution into two 1D distributions demonstrated for  $\sin(x)^2 \text{rect}(y)$ . Notice that throughout this thesis the rectangular functions were in fact modified to a trapezoidal shape with a ramp of 8 pixels at the ends. As the algorithm is having trouble with sharp edges this measure increases the smoothness of the simulated patterns.

27. One-dimensional reduction works because the Fourier transform (equation 30) will then also be of separable form.

$$I_t(x) \cdot I_t(y) = |\mathfrak{F}[\sqrt{I_i(x) \cdot I_i(y)} e^{i\Phi(x,y)}]|^2 \quad (49)$$

$$= |\mathfrak{F}[\sqrt{I_i(x)} e^{i\Phi(x)}] \cdot \mathfrak{F}[\sqrt{I_i(y)} e^{i\Phi(y)}]|^2. \quad (50)$$

After calculating a phase distribution for each dimension the total phase pattern in 2D can be simply reconstructed:

$$\phi(x, y) = \phi(x) + \phi(y). \quad (51)$$

Fourier transforming this phase pattern with the input amplitude profile yields the desired reconstructed target.

In theory this method should allow for tweaking the phase calculation such that the recomposed targets are more homogeneous.

Proceeding like this limits the available degrees of freedom for the phase pattern to a subset. This has the advantage that the computation time of the Fast Fourier transforms is significantly reduced since the complexity simplifies to  $\mathcal{O}(N_x \log_2(N_x))$  and  $\mathcal{O}(N_y \log_2(N_y))$  respectively.

Usual iteration numbers are on an order of magnitude of ten thousands and are computed in less than a minute.

Using this methods produces simulated sinusoidal patterns with an impressively low RMSE as presented in the next section could be achieved. These simulations are largely independent of the initial

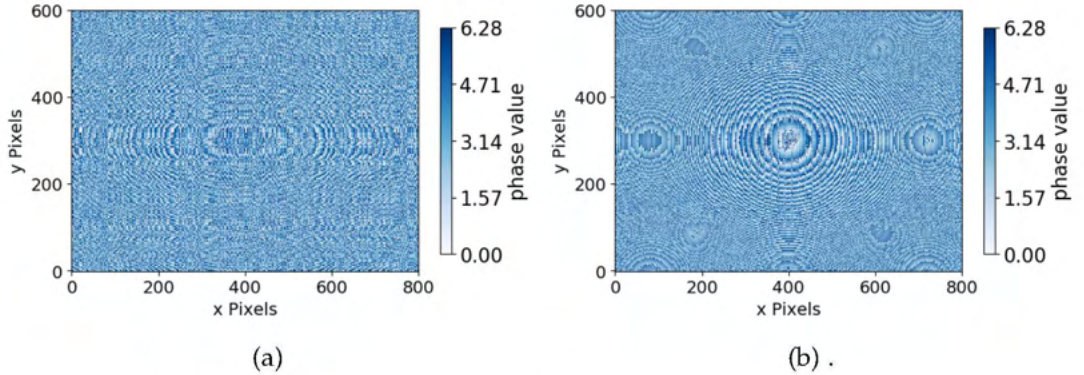


Figure 28: Phase patterns for a sinusoidal target resulting from 1D (a) and 2D (b) calculations. The latter shows a smoother phase distribution than the first.

guess as speckles do not appear in one-dimensional IFTAs, but have the disadvantage of a reduced efficiency in comparison to the two-dimensional MRAF.

These one-dimensional computations could also be extended to isotropic targets, meaning targets of the form  $I(x, y) = I(r)$  with  $r = \sqrt{x^2 + y^2}$ , which could be used e.g. for radial  $\sin^2$ -patterns like mentioned in the research plan section. Also separability in polar coordinates could be used for targets of the form  $I(r, \theta) = I(r) \cdot I(\theta)$  with  $\theta = \arctan(y/x)$ .

Nevertheless, one has to stay sceptical and ask if these almost perfect simulations also bear scrutiny in an experimental setup. Since one-dimensional calculations are automatically more prone to an input deviating from the theoretical assumption, unexpected fringes may appear [8, 26]. Furthermore, the considerations about the second type of  $\pi$ -phase jump speckles may be of relevance in practice. The resulting total phase patterns seems to contain strongly fluctuating phases in adjacent regions, that, propagated into the Fourier plane, could at least lead to attenuation of the intensity in between two real-world focal spots (see figure 25). Compared to 2D MRAF calculations the phase patterns are less smooth as shown in figure 28.

#### 4.6 CONCLUSION AND VERSATILITY DEMONSTRATION

Making use of this knowledge about the MRAF algorithm it is now possible to reproduce desired intensity distributions to a very high accuracy. The introduction of an amplitude freedom region allows for significantly increased quality of the simulations to the cost of a lower light utilization efficiency.

This simulation quality is demonstrated by a selection of results for sinusoidal targets in table 1. They were performed for patterns

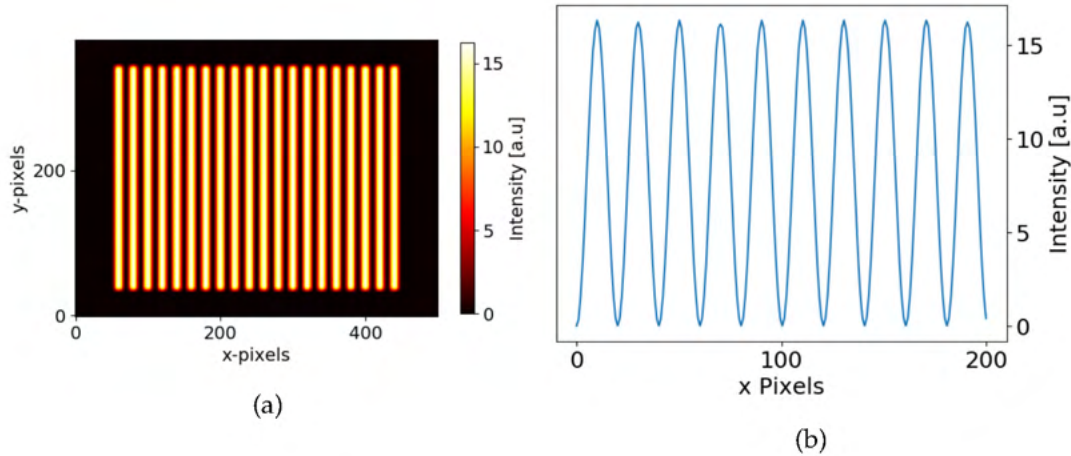


Figure 29: Simulated sinusoidal target with 20 focal units peak to peak distance (a) and a horizontal cross section (b). The simulation has a RMSE of 3%. Especially the cross section shows the accuracy of the simulated pattern.

Table 1: Exemplary simulation values for  $\sin^2(x)$  targets calculated by means of the 2D and 1D MRAF

peak to peak [f.u.]	2D		1D	
	RMSE [%]	efficiency [%]	RMSE [%]	efficiency [%]
40	3.5	45 (m=0.4)	2.45	17 (m=0.5)
10	3.3	18 (m=0.3)	2.46	17 (m=0.5)
4	5.1	17 (m=0.3)	2.86	4 (m=0.4)

of a size  $400 \times 300$  on a total canvas of size  $1600 \times 1200$  (due to the Nyquist-Shannon theorem), meaning that in the real experiment all the sizes like the periodicity are actually halved. Due to the diffraction limit of the simulations it is only possible to go down to 4 pixels peak to peak distance in sinusoidal patterns.

The cross sections through the simulated targets perfectly show the desired sinusoidal shape, similarly good both for large and small peak to peak distance, therefore only one of the crossections is displayed in figure 29.

It needs to be tested if the one-dimensional calculation will in practice yield better results and if we are actually able to experience the single-digit quality differences, or if due to the errors in the experimental set up actually the quality difference is negligible.

Circular sine targets can also be created with the MRAF-algorithm, but show a higher RMSE because of discretisation effects along the rings, here reasonable results can be obtained until a shortest peak to peak distance of 12 focal units, see table 2.

Table 2: Simulation values for  $\sin^2(r)$  target

peak to peak [f.u.]	RMSE [%]	efficiency [%]
40	4.8	44.5 (m=0.4)
20	12.5	18 (m=0.3)
12	20.5	19 (m=0.3)

The RMSE values can be further tweaked by selecting other noise masks and adjusting the target size. In the end one will have to choose a proper size with respect to the desired size in the experiment, because too large simulated targets will cause light to be waisted, meaning that the shaped light distribution will have a smaller intensity in the relevant region.

If one is interested in generally improving the MRAF the offset-MRAF (OMRAF) algorithm [36] could be investigated, where an additional global background intensity is added to the targets. This reduces the RMSE even further because the IFTA is then not forced to create problematic regions of zero intensity. Like this also the problematic radial sinuses can be recreated with only a few percent RMSE. Nonetheless an intensity background is probably not suited for our final experiment, even though it could be discussed if a small offset (usually 10% of the maximum amplitude, which is equivalent to 1% of the intensity) would be acceptable.

I would like to conclude this chapter by demonstrating that the MRAF is also able to reproduce more complex patterns, therefore in figure 30 a series of simulations is shown. Obviously the use of these patterns in a future Rydberg atoms experiment can be strongly doubted, but actually shaping a real laser beam into these patterns would for sure be an impressive demonstration of power of the SLM.

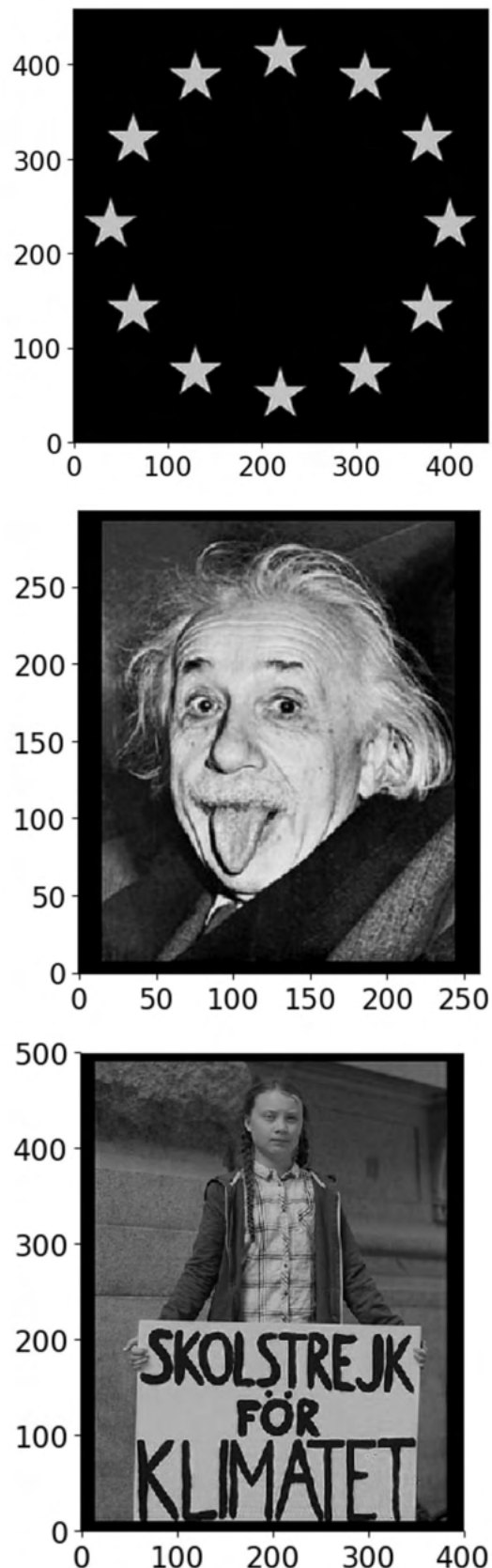


Figure 30: Three complex intensity distributions recreated with the MRAF-algorithm



# 5

## PRACTICAL IMPLEMENTATION AND MEASUREMENTS

---

Up to now all our considerations were of purely computational nature. They helped us creating phase patterns that we are now going to test with our SLM. The central question that arises now is, to which precision will the simulations be recreated with the laser light.

This chapter starts by describing the used experimental setup and will then focus on how to overcome the aberrations and other problems that are deteriorating the quality of the shaped light patterns.

### 5.1 OPTICAL SETUP

The optical setup to investigate the basic functionalities of the SLM is kept simple in order to minimize error sources, as is shown in figure 31.

After leaving the fiber (1) the collimated 780nm laser beam of a power of  $\sim 50\mu\text{W}$  is sent through a half-wave plate (2) and a polarizing beam splitter (3) such that its intensity can be modulated in a certain range. To function properly the light incident on the SLM should be polarized in the direction of the liquid crystal molecules. The beam is then widened by a telescope (4) by a factor of 8 to make use of the entire capabilities of the SLM with respect to the resolution of our imaging system (equation 25).

Item (5) is the Hamamatsu spatial light modulator. After having been phase-modulated the light passes an achromatic doublet lens of diameter 50.8mm (6) with focal length 150mm which performs the Fourier transform. The mirrors (7) allow for accurately aligning the beam on the SLM. Following the instructions by the SLM-manufacturer the incident angle of the beam is chosen small (the angle should not surpass 5 degrees). The focal length will define the pattern size on the CCD-camera (8).

The Fourier plane is finally displayed with CCD-camera from AVT (Stingray F125) (8), whose semiconductor-chip has a resolution of 1292(H)  $\times$  964(V) pixels, the individual pixel-size amounting to  $3.75\mu\text{m}$ . For easily adjusting the Fourier plane position on the camera another mirror is implemented in the setup.

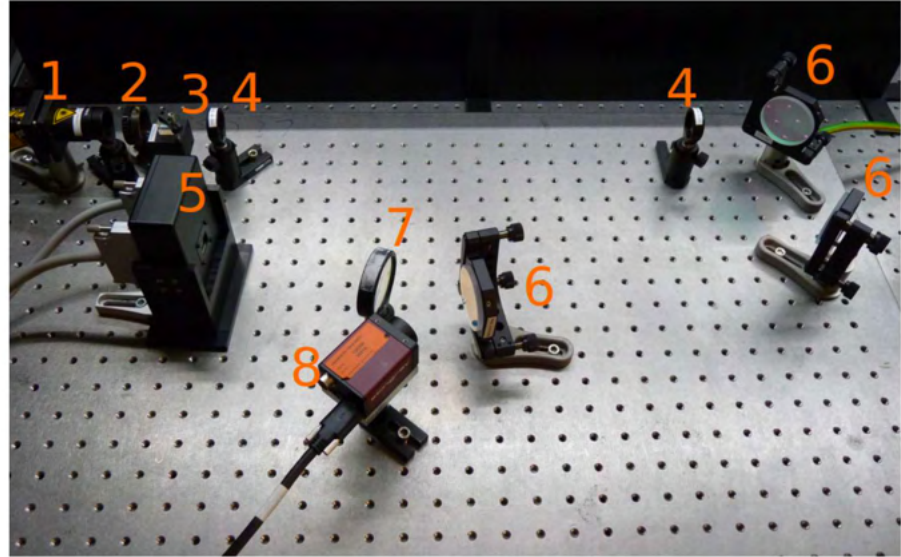


Figure 31: Setup in the lab used to investigate the functioning of the SLM, for component description see the text.

## 5.2 ABERRATION CORRECTION WITH A SPATIAL LIGHT MODULATOR

The central problem that arises when trying to display certain images with the SLM are optical aberrations. As can be seen in figure 32a the sinusoidal target whose error in the simulations was on the scale of a few percent is now distorted. The effect of the aberrations protrudes even more if we try to generate an array of spots. In figure 32b a  $10 \times 10$  grid is not at all recognisable on the CCD. It is not a surprise that the finely structured light patterns are heavily distorted by aberrations, as all optical devices introduce aberrations to a greater or lesser extent, even in the current basic setup. Especially in the final experimental setup with its vast number of lenses and mirrors these effects will probably be significantly stronger. As a consequence one will not be able to reach the full resolution of the imaging system and the final target quality will be severely decremented, especially for continuous targets.

It is therefore essential to develop methods to characterise the aberrations and at best tackle them directly with the SLM without being forced to alter the entire setup. This section presents one way to achieve this, following the work done by *van Bijnen* [8, 37] and initiated by *Bowman* [38].

### 5.2.1 Disturbance of the wave front

In light of the fact that with a SLM-device we are performing phase modulation in a Fourier optics setup, aberrations can be approxi-

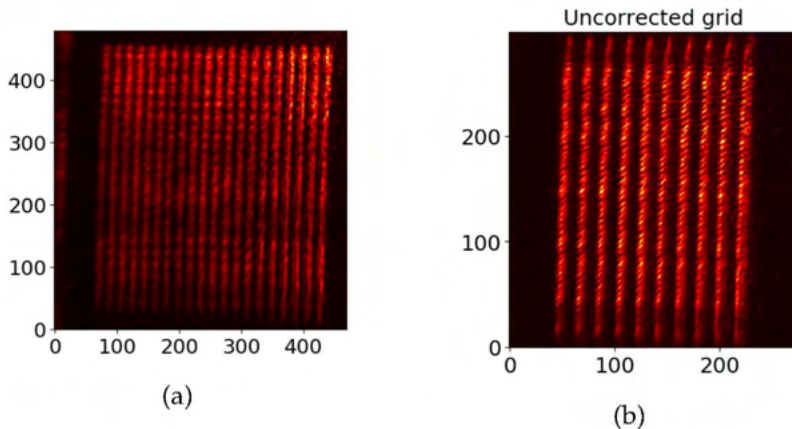


Figure 32: Influence of aberrations. In figure a) a  $\sin^2$  and in figure b) a  $10 \times 10$  grid of spots should be displayed. The need for aberration correction is obvious.

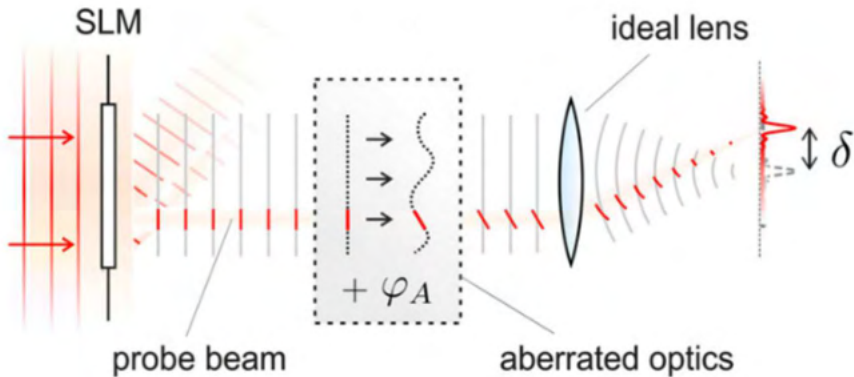


Figure 33: Additional phase  $\phi_A$  due to aberrations, from [37].

mated as local tilts of the wave front (the surfaces of equivalent phase). These unwanted distortions will add up to the phase intentionally added by the SLM while the light is travelling along its beam path as illustrated in figure 33.

Assuming that light at a certain position  $(x, y)$  in the plane perpendicular to the light propagation direction will stay approximately at this position the starting situation may be stated as follows:

$$\phi(x, y) = \phi_0(x, y) + \phi_A(x, y) \quad (52)$$

with  $\phi_0$  being the phase pattern displayed on the SLM and  $\phi_A$  being the additional phase due to aberrations.

Hence, determining  $\phi_A$  would allow for subtracting it to  $\phi_0$  in the SLM-plane in order to compensate for the aberrations.

### 5.2.2 Zernike polynomials

In order to reconstruct  $\phi_A$  it is necessary to use a sequence of polynomials which on the one hand create a smooth phase correction pattern and on the other hand are able to inform us about the underlying aberrations of the optical system. To that end Zernike polynomials are a powerful tool. They form a continuous set of orthogonal polynomials on the unit disk, orthogonality implicating that they are independent of each other [39]. The advantage of Zernike polynomials over all other infinite sets of polynomials on the unit disk is that the first polynomials represent classical types of aberrations like coma, astigmatism and defocus.

As the area defined by the SLM is rectangular and not circular, the original Zernike polynomials cannot be used. Therefore we have to draw on Zernike polynomials calculated for non-circular apertures like rectangles as presented in [40]. The principle consists of setting the rectangular aperture perfectly in the unit disk such that the corners coincide with the unit disk margin, thus the aspect ratio of 600/800 pixels is the defining factor in our case. After measuring the aberrated wave front,  $\phi_A$  is fitted by decomposing it into a linear combination of the first 15 Zernike Polynomials  $Z_n$ , the magnitude of the coefficients  $c_n$  telling us which types of aberrations are dominating.

$$\phi_A(x, y) = \sum_{n=1}^{15} c_n \cdot Z_n \quad (53)$$

The fitting procedure itself consists of solving a linear equation system represented by the following matrix equation:

$$\underbrace{\begin{bmatrix} Z_1(x_1, y_1) & Z_2(x_1, y_1) & \dots & Z_{15}(x_1, y_1) \\ Z_1(x_2, y_1) & \ddots & \dots & Z_{15}(x_2, y_1) \\ \vdots & \dots & \ddots & \vdots \\ Z_1(x_{800}, y_{600}) & Z_2(x_{800}, y_{600}) & \dots & Z_{15}(x_{800}, y_{600}) \end{bmatrix}}_A \cdot \underbrace{\begin{bmatrix} c_1 \\ c_2 \\ \vdots \\ c_{15} \end{bmatrix}}_C = \underbrace{\begin{bmatrix} \phi_A(x_1, y_1) \\ \phi_A(x_2, y_1) \\ \vdots \\ \phi_A(x_{800}, y_{600}) \end{bmatrix}}_B \quad (54)$$

On the left hand side a matrix A consisting of the first 15 Zernike polynomials evaluated for every pixel in one row is multiplied by a column vector C containing the 15 Zernike coefficients. On the right hand side the measured phase aberrations are represented as a column vector B. Thus the fitting procedure consists of finding an inverse matrix of A with the least square method and multiplying it with the phase aberration vector B.

$$C = A^{-1} \cdot B \quad (55)$$

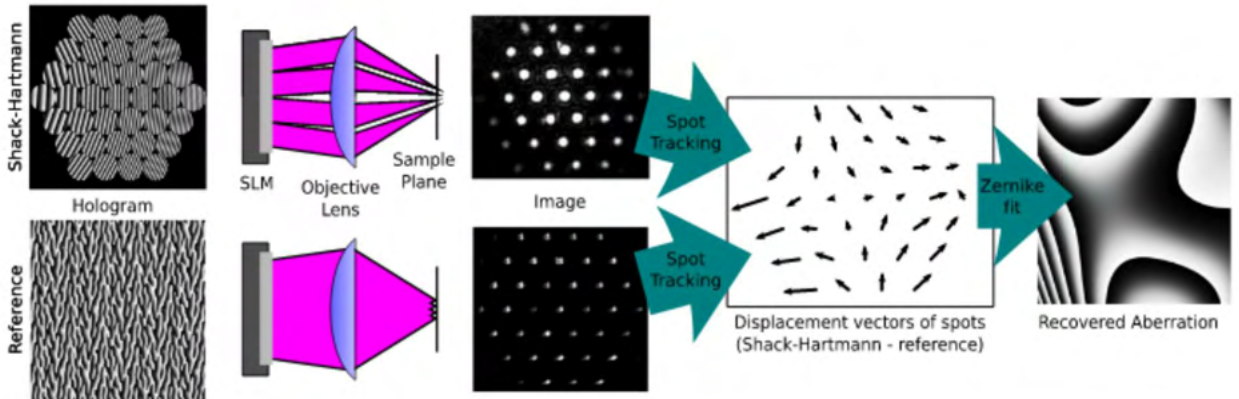


Figure 34: Mimicking a Shack-Hartmann wavefront sensor with an SLM as proposed in [38]. The reference pattern is computed with an IFTA, here the local position shifting is canceled because the light for every spot originates from the whole SLM.

### 5.2.3 *Shack-Hartmann algorithm*

The method implemented in this thesis takes its name from Shack-Hartmann wavefront sensors which have been developed for aberration determination of astronomical telescopes in a field known as adaptive optics. The sensors help to counteract the influence of atmospheric optical turbulence. The method consists of letting the incident light pass an array of lenses, consequently the light is focused into an array of spots. The aberration now cause the spots to be at altered positions in contrast to the theoretical prediction.

This concept has been picked up by Bowman [38] and applied to SLMs. An array of lenses can be mimicked by segmenting the SLM into an array of circles which are imprinted with a certain linear gradient. As was presented in section 2.3.3 a linear gradient causes a shift of the spot in the image plane. Each circle now acts as a circular aperture and the different linear gradients will cause the Fourier-transform of the SLM-Plane to be an array of spots as illustrated in figure 34. The spot size itself is governed by the diffraction-limit for such Airy-discs of equation 24, where the size of the central maximum is inversely proportional to the circle radius. Consequently the light for each spot array only comes from one respective SLM area.

*Van Bijnen* [37] developed this idea further. The proposed method breaks down the concept of an array of lenses to examination of only one of those circles on the SLM at a time as depicted in 35a. Such an investigation will need more time but allows for a more precise analysis of the SLM.

The phase pattern needed for this method consists of dividing the SLM into a circular area and its exterior. The circle is imprinted with a linear gradient in order to separate the light originating from that SLM apart from the rest. This circle will automatically move over the surface of the SLM first vertically and horizontally and each time the aberration for the specific SLM part is going to be measured. Instead of imprinting the circle with a linear gradient it is also conceivable to do the opposite and leave the circle without a linear gradient. As long as the region of interest for detecting the spot is chosen correctly there is no difference.

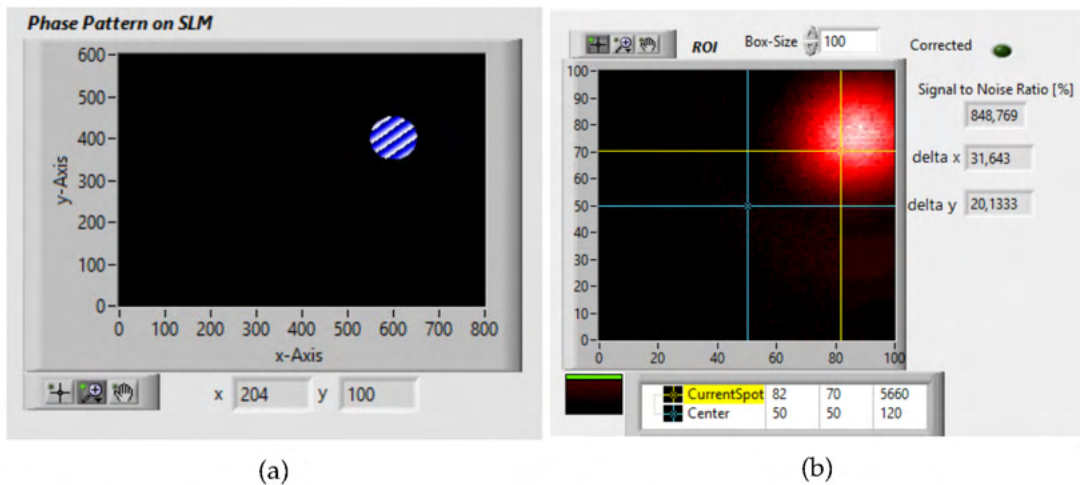


Figure 35: Phase pattern used for examining SLM parts (a) and automated spot detection in the camera image in the LabVIEW-program (b).

The quantity that is now measured is the displacement of each spot for every part of the SLM that is examined, because for an ideal aberration free setup these spots should all be at the same location according to Fraunhofer diffraction. In order to define a displacement as a reference location the spot position for the circle in the centre of the SLM is set. Spot detection while the circle is moving over the SLM can be simply automated by a centre of mass calculation without the camera background noise in a predefined region of interest, as shown in figure 35b.

Of course if the entire SLM is examined at a time and no special phase pattern is imprinted the local displacements are canceled out, but as soon as the calculated phase patterns for certain targets are imprinted this is not the case any longer, that is why such a measurement makes sense.

As mentioned before the spot displacements can be interpreted as phase gradients in the SLM-plane, such that for each small SLM sam-

ple we reconstruct  $\phi_A$  locally as a gradient around the center of the circles  $(x_0, y_0)$

$$\phi_A(x_0, y_0) = \nabla\phi_A(x_0, y_0)(x - x_0, y - y_0), \quad (56)$$

Calculating the according linear gradient to reconstruct  $\phi_A$  revisits the dimensional considerations in section 2.3.3 of this thesis. A shift of  $(x, y)$  needs to be converted into focal units  $\Delta x$  and  $\Delta y$  taking into account the camera pixel size  $\Delta_{cam}$ , meaning that we have to calculate  $\frac{x \cdot \Delta_{cam}}{\Delta x}$  and  $\frac{y \cdot \Delta_{cam}}{\Delta y}$  respectively.

The Shack-Hartmann procedure can be summarized by four basic steps

1. A circle on the SLM is imprinted with a linear phase gradient.
2. The Airy spot created by this circle is detected in the camera image.
3. The displacement of this spot to the reference position is determined and translated into a linear phase gradient. This linear phase gradient corresponds to the aberration on that part of the SLM.
4. The circle on the SLM moves on to the next location and continues iteratively with step 2.

This method is obviously limited by the radius of the moving circle because the calculation will assume one linear gradient for that entire SLM-segment. Due to the growing Airy disc size and the diminished intensity a radius of at least 40 pixels is needed. In order to achieve a reconstructed phase pattern that can be fitted smoothly with Zernike Polynomials a step size of 20 pixels proves to be adequate. As the areas of the SLM are sampled several times due to the overlap of the circles an average linear gradient for each region can be computed.

This averaging has the effect that in the end the displacements are widely reduced but never completely vanish. In practice it has also become clear that the reduction of the displacements, that is the aberrations, can be minimized by not applying the full correction at a time, but by only taking 0.5 of the actual gradient and instead let the algorithm run at least two times over the SLM. For the reconstruction of the phase pattern the modulo of 256 due to the discretised phase levels of the SLM should of course only be taken after fitting with Zernike polynomials.

### 5.2.4 Aberration correction

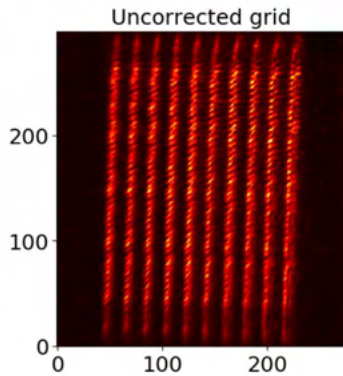
Now that the principle of this method of aberration correction has been laid out the results of this procedure can be presented. As it is recommended to always use the correction pattern provided by the manufacturer we used it as a set background throughout the measurements.

The aberrations persisting in this uncorrected situation can be depicted by deviation maps of the SLM surface as shown in figure 36. These heatmaps show how the spot deviations vary on the surface of the SLM in x and y direction respectively. The information contained in these maps can be further visualised by histograms of the displacements. If the algorithm is successful it should be able to largely reduce the width of the histogram values. After the first measurement on the SLM surface horizontal and vertical displacements of the spots ranges over several focal units.

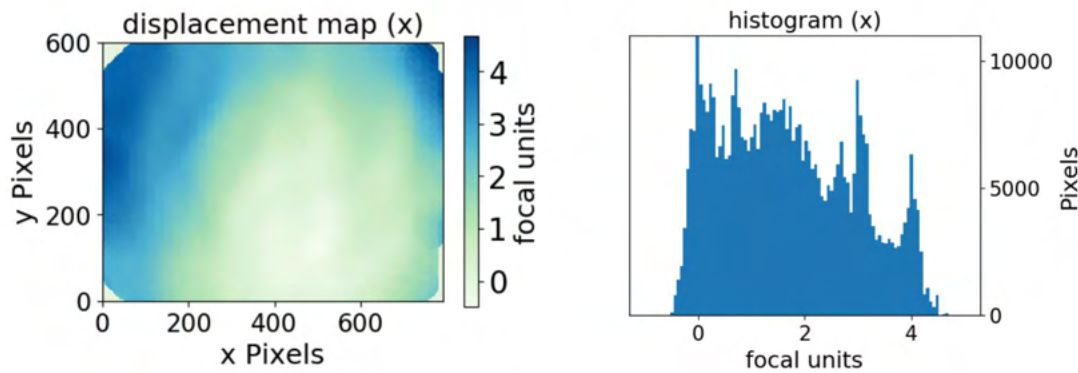
We let the algorithm correct the aberrations three times in a row and at each time use the correction pattern that was generated the time before as a background. This allows for largely reducing the aberrations as is shown in figure 36. The heatmaps that use the same colorscales as before are now more homogenous and the range of displacements decremented by a factor of 4 and 16. Applying the final correction pattern (see figure 38) to the SLM finally makes the grid of spots visible (see figure 36). Nevertheless the grid still contains some aberrations.

Another interesting application for this aberration correction method is to see whether it is able to recover the correction pattern provided by the manufacturer. To that end correction runs without the Hamamatsu pattern (see figure 7b) were carried out. In figure 38 the result can be compared to the correction pattern where the Hamamatsu pattern was already applied. A resemblance is identifiable. Actually it is hard to tell which of them does the better aberration correction, as the displacements are similarly diminished and the corrected grid of spots looks alike.

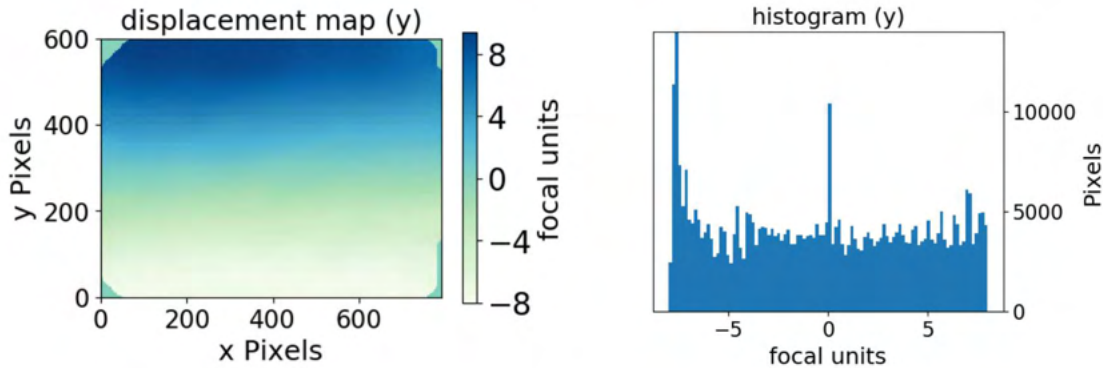
To finish this section about aberration correction it should be considered how this method could be used in the final experimental setup with Rydberg atoms. One may think that the presented method is useless, because it will not be possible to place the camera in the plane where the atoms are going to be trapped. It is thus worth mentioning that the method was specifically designed for setups with ultracold atoms and actually has been tested in a magneto-optical trap, where ions were used as the displacement indicator to reconstruct the phase aberration [37]. According to the same publication the correction performance works near the diffraction limit. The Shack-Hartmann



(a)  $10 \times 10$  grid of spots, which is not recognisable due to aberrations.

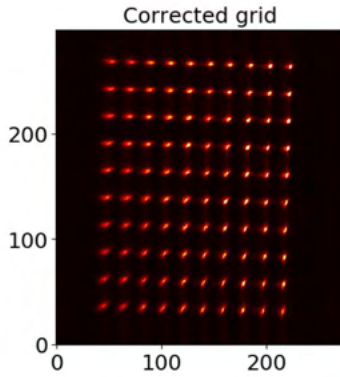


(b) Measured horizontal spot displacements during first run of the SH algorithm. The measured values at the corners were omitted due to the low signal to noise ratio of the detected spots.

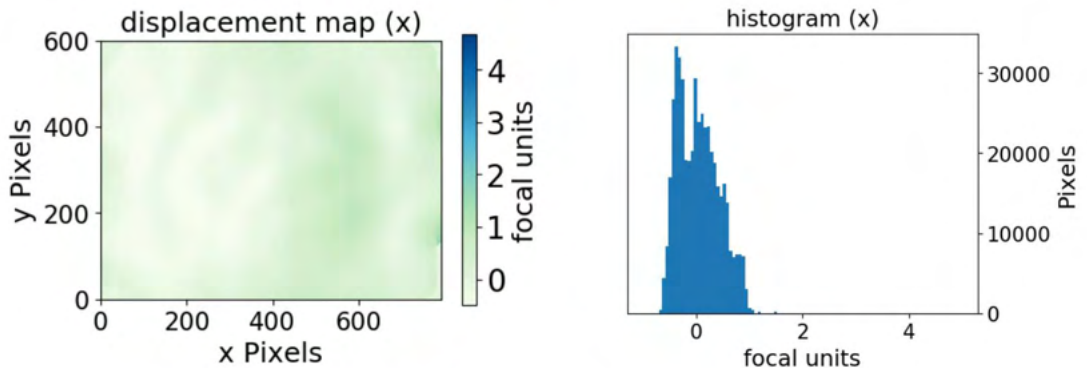


(c) Measured vertical displacements during first run of the SH algorithm.

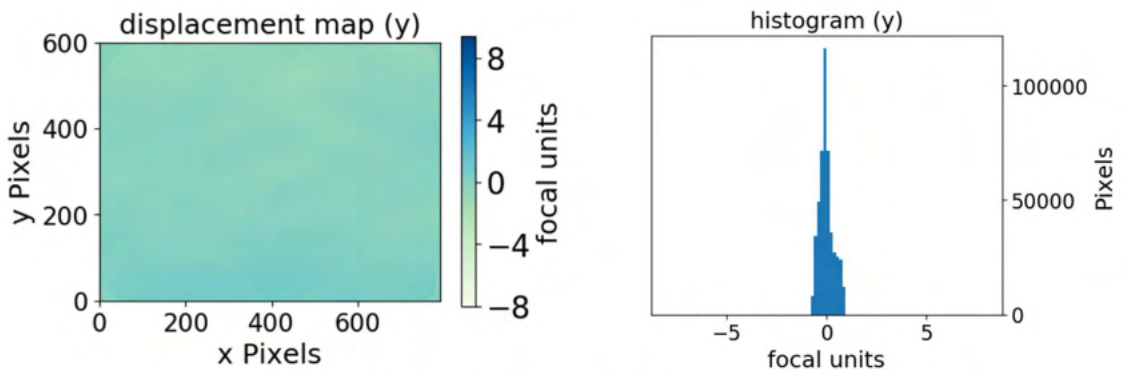
Figure 36: Initial aberration situation without any correction. The displacements of the Airy spots over the SLM are displayed in the form of heatmaps and the corresponding histogram. The aberrations cause displacements of several focal units.



(a) Grid of spots after application of the computed correction phase pattern.



(b) Measured horizontal displacements after three runs of the SH algorithm.



(c) Measured horizontal displacements after three runs of the SH algorithm.

Figure 37: Situation after three consecutive runs of the SH algorithm. With the computed correction pattern the displacements in comparison to the initial situation (figure 36) are diminished by a factor of 4 and 16 respectively. With the same colorscale as for the initial situation the maps of the SLM are now mostly homogeneous. The grid of spots can be displayed on the CCD.

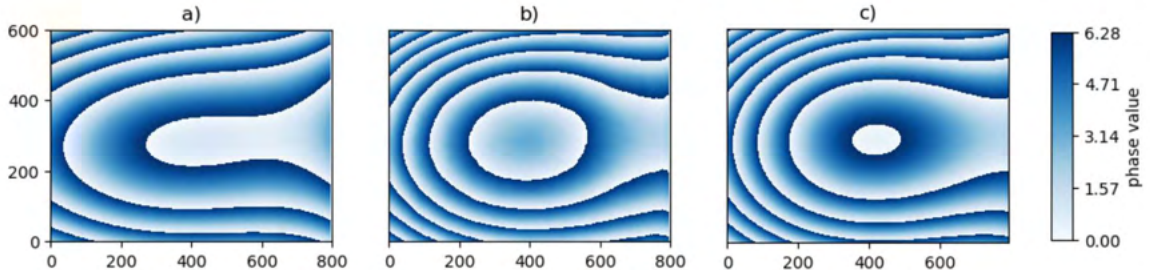


Figure 38: Correction patterns measured with the Shack-Hartmann algorithm. Figure a) is the retrieved phase pattern that was obtained in the first place, the Hamamatsu correction pattern was used as a background (figure 8).  
 Figure b) is the combination of a) and the Hamamatsu pattern.  
 Figure c) displays the full correction pattern that was retrieved without the Hamamatsu pattern as a background.

algorithm that I built should be further investigated with regard to such phase error metrics.

### 5.3 AMPLITUDE RECONSTRUCTION IN THE SLM PLANE

As has been depicted in section 4.4 a faulty estimation of the initial amplitude in the SLM plane may cause the otherwise precisely calculated phase patterns to produce deficient inhomogeneously illuminated intensity patterns in practice. A precise alignment on the small SLM-chip without further means –especially after the beam has been widened– is not that easy. Fortunately, this problem can be easily handled by a small adaptation of the Shack-Hartmann algorithm.

Using the same method of examining small circular apertures on the SLM the intensity of the resulting spot in the Region of Interest of the CCD-camera image is measured. With these intensities and an exact scanning a relative intensity phase pattern can be reproduced. Figure 39a illustrates such a reconstructed relative amplitude for an already calibrated setup. The pattern looks Gaussian, although it seems to be flawed by some bumps at the side. As these bumps were reproduced by several amplitude reconstruction runs, the laser should be investigated with a laser beam profiler.

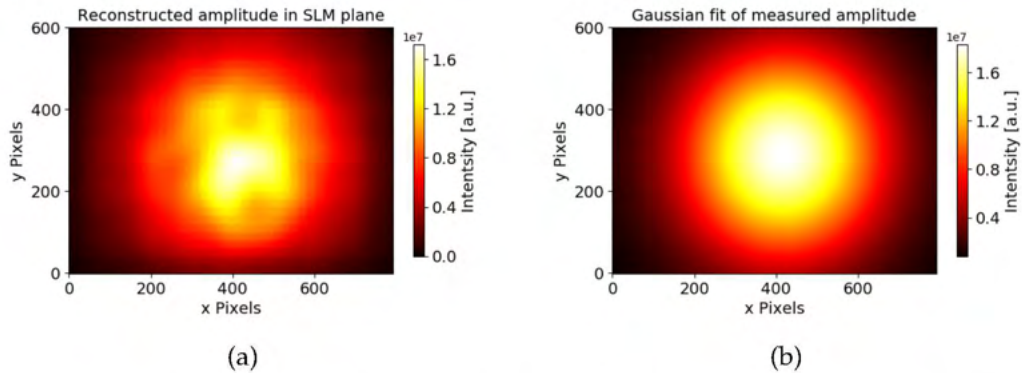


Figure 39: Reconstructed amplitude in the SLM plane. Figure a) displays the actual measurement and figure b) the Gaussian fit which allows for determining the beam specifications needed for the correct phase pattern calculations.

A Gaussian fit is now applied to this data, providing us with fit-parameters like width and position, which can then be used for precise calculation of phase patterns with the MRAF algorithm. After a few adjustments with the mirrors satisfactory values can be obtained. In this case these are a centre position of  $x=390$  and  $y=400$  pixels and a Gaussian beam width of 263 pixels.

It is worth mentioning that for this calibration the linear gradient used to shift the observed spot should not be chosen to large, as this will lead to intensity fluctuations on a time scale of the refresh-rate of the SLM, as has been investigated in [10]. Needless to say, this effect can be hedged in by taking several images for each spot and averaging the measured intensities. Nevertheless it is recommended to use a laser intensity as stable as possible for an exact relative amplitude measurement. A large linear gradient necessary to shift an intensity pattern can still be added after this adjustment.

## 5.4 EXPERIMENTAL MEASUREMENTS

Finally we can proceed with showing actual measurements of the sinusoidal patterns recorded with the CCD. However, even after aberration correction one central issue remains, the light that cannot be modulated by the SLM.

### 5.4.1 The zero-order spot

In figure 4o the phase pattern for a sinusoidal target including all correction patterns was applied to the SLM. The resulting pattern is largely outshined by one central bright spot in the middle. In fact the desired sinusoidal target is only visible in this image, because the intensity is saturated for the central spot. In addition it looks like some

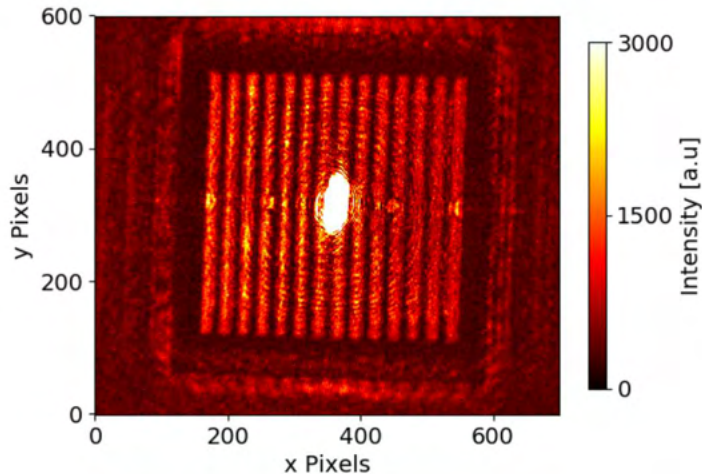


Figure 40: Influence of the zero-order spot without any applied shifting linear gradient. The intensity of the CCD in the zero-order spot is chosen to be saturated in order to make the actual pattern visible. In addition to the bright center point a kind of concentric interference pattern is visible, whose influence can persist, even if the pattern is shifted away with a linear gradient.

kind of destructive interference pattern is propagating in form of concentric circles away from this central spot. This is a well known defect of SLMs, the so called zero-order spot. It originates from the fact that the SLM chip is not entirely covered with pixels. The incident light that is reflected in between the pixels cannot be modulated and thus always focuses into this spot which remains at the same place. Of course in the final experiment this spot cannot be tolerated and needs to be avoided.

A first approach to avoid it simply consists of adding a linear phase gradient to the SLM such that the target intensity is shifted away, this is actually what was done for making the images presented in the aberration section possible.

Unfortunately, just using a linear gradient is not enough. It can be observed that imprinting a large linear gradient also affects the quality of the targets (a new correction pattern should be measured for that shifted central position). In addition as the zero-order spot is always focused at one spot it appears brighter than the shaped targets, because in addition to the extent of the targets some light is already thrown away due to the MRAF principle in dependence of the mixing factor. A fact that increases its influence is that it is actually defocused in comparison to the intensity patterns. The applied aberration correction patterns to some extent act like a lens which is shifting the focal point in the light propagation direction. This can be seen in figure 41 where the camera was positioned such that the sinc-spot of the

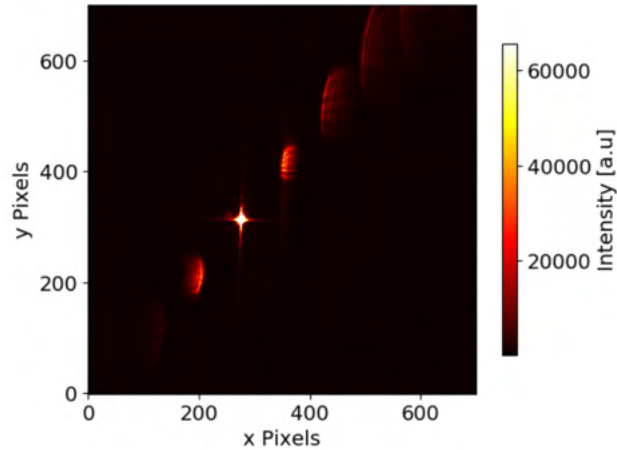


Figure 41: Defocused zero-order spot next to the sinc-spot of the SLM at position (400,400). In addition some higher (defocused) diffraction orders of the sinc-spot are visible. The higher diffraction orders and the zero-order spot being out of focus has the effect that we see an image of the diffraction plane, meaning the SLM. The sinc-spot is largely saturated in order to make the unmodulated light visible.

SLM is in focus. The neighbouring zero-order spot has a rectangular shape because this is actually an image of the SLM surface. For this kind of image the sinc-spot needs to be saturated, such that the the zero-order spot is also visible, therefore it is made certain that the zero-order spot only contains a small percentage of the light.

If the sinusoidal target is shifted out of the zero-order spot it can be observed that the pattern illumination becomes inhomogeneous with a clear bias towards the zero-order spot. Especially targets with a smaller periodicity are affected by this as shown in figure 42.

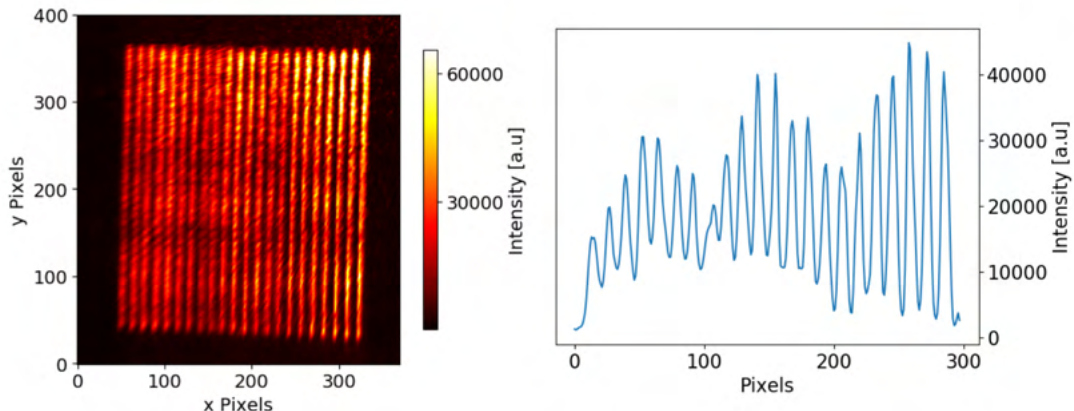


Figure 42:  $\sin^2$  target with 7 focal units periodicity and corresponding cross section

I also performed some flatfielding measurements to test if the different CCD pixels' responsivity may be a source of trouble in our setup. Flat fielding is performed by homogeneously illuminating the CCD chip through a diffusor and then measuring the responsivity of each pixel. A master flat field is then created by normalizing the pixel values such that the median response of each pixel is one, but in this regard our CCD is apparently not the problem. All pixels had a responsivity close to 1.

#### 5.4.2 *First approach to avoid the zero-order spot*

Towards the end of my project I tried to build a set up where the zero-order spot is spatially filtered out. To that end one can spatially separate it from the target with a linear gradient in an intermediate Fourier plane. There the unmodulated light can be blocked with an aperture. We then need to lenses in order to recreate the Fourier image for the CCD. This is then a 6f setup, see figure 43. This eliminates the bright zero-order spot from the field of view of our camera, such that the laser intensity can be set higher in order to make the images more visible. Due to the additional lenses the shaped intensity patterns are now more aberrated than before, but we can make use of the Shack-Hartmann algorithm in order to find a correction pattern. For the reconstruction of the aberrated wavefront it is important to know the new focal unit that has been changed by the additional lenses. After performing aberration correction at this displaced location, the  $10 \times 10$  grid is more aberrated than after the correction in the initial position. Apparently this method comes at the cost of introducing additional aberrations, that cannot fully be recovered by the Shack-Hartmann algorithm.

In the future more sophisticated methods to avoid the zero-order spot should be tested, for instance one could use lens-like phase patterns in combination with linear gradients as suggested in [41]. I suppose that the images would also be optimised if the shifted target is already taken into account in the MRAF calculations instead of adding a linear gradient afterwards.

#### 5.4.3 *Pattern measurements*

Apart from the problems arising in the setup, it is of interest to actually measure the desired intensity patterns. For a discrete grid we have already shown, that the aberration program enables us to do so.

Up to now, the program is not able to directly map between the image and the target for which the implemented phase pattern was initially calculated, so we remain at simply looking at the CCD image

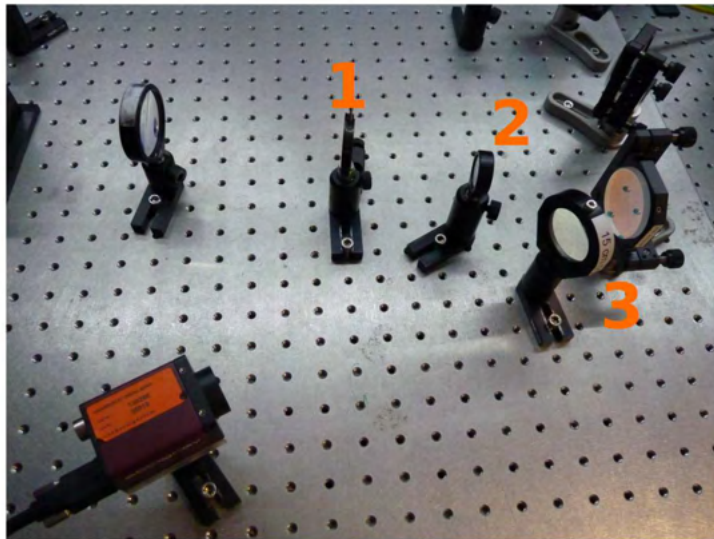


Figure 43: New 6f setup in order to filter zero-order spot. In an intermediate Fourier plane an aperture (1) is placed such that the zero-order spot can be blocked after the target has been displaced with a linear phase gradient. The lenses (2) and (3) are needed for reconstructing the Fourier image in the camera plane.

and cross sections of the periodic targets. In the long run some mapping procedure between the camera image and the simulated patterns has to be implemented in order to calculate a RMSE.

In figure 45 a range of created light patterns after spatial filtering of the zero-order spot is displayed. The patterns are now less noisy than before and also small scale sinuses show their typical periodicity, although they are still more peaked than sinusoidal. Apparently the used linear gradient is not large enough, and illumination inhomogeneities towards the zero-order spot persist. A contrast analysis of peaks and sinks of the targets is thus not informative yet. At this point it is not possible to recreate some more complex patterns like Einsteins tongue photo that is barely recognisable (figure 45).

Concerning the comparison of the phase patterns calculated in one or two dimensions there are some distinguishable differences as is displayed in figure 45d. The one-dimensional patterns seem to produce larger inhomogeneities and fringes in the light patterns, which could originate from the more fluctuating phase distribution or higher sensitivity to aberrations. At this stage further investigation in this direction were omitted. All measured targets originate from phase patterns computed in two dimensions.

An additional experimental problem is the occurrence of ghost copies behind the targets (see figure 44) which is probably one cause for image quality deterioration. As hinted by *van Bijnen* [8], this can arise because the SLM also slightly modulates the amplitude dependent on the applied phase for each pixel. It remains to be investigated,

whether this is a major reason for the sinusoidal patterns to be degraded.

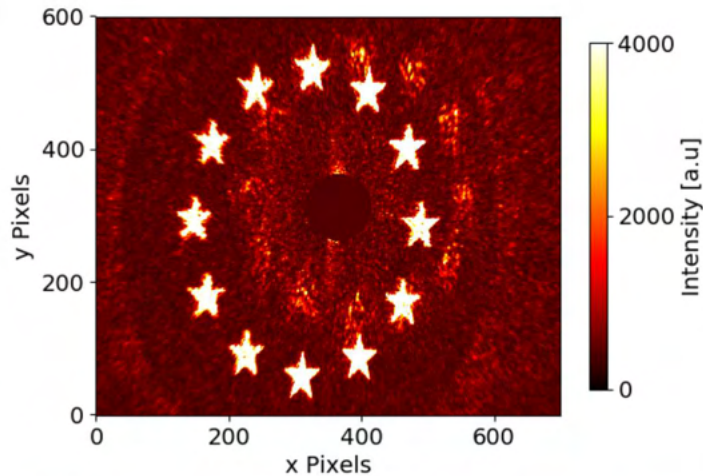


Figure 44: Ghost copy of a pattern in the background. It is made visible through a small displacement of the target and by taking a high contrast image. The overlap between a target and its ghost copy might affect the image quality. The zero-order in the centre was blocked by a digital mask.

In this chapter it was shown, that the SLM can be used to mitigate the influence of aberrations and an improper beam alignment on the SLM. Nonetheless, in our setup a set of other problems persist. The high accuracy of the phase generating simulations could not be reached yet.

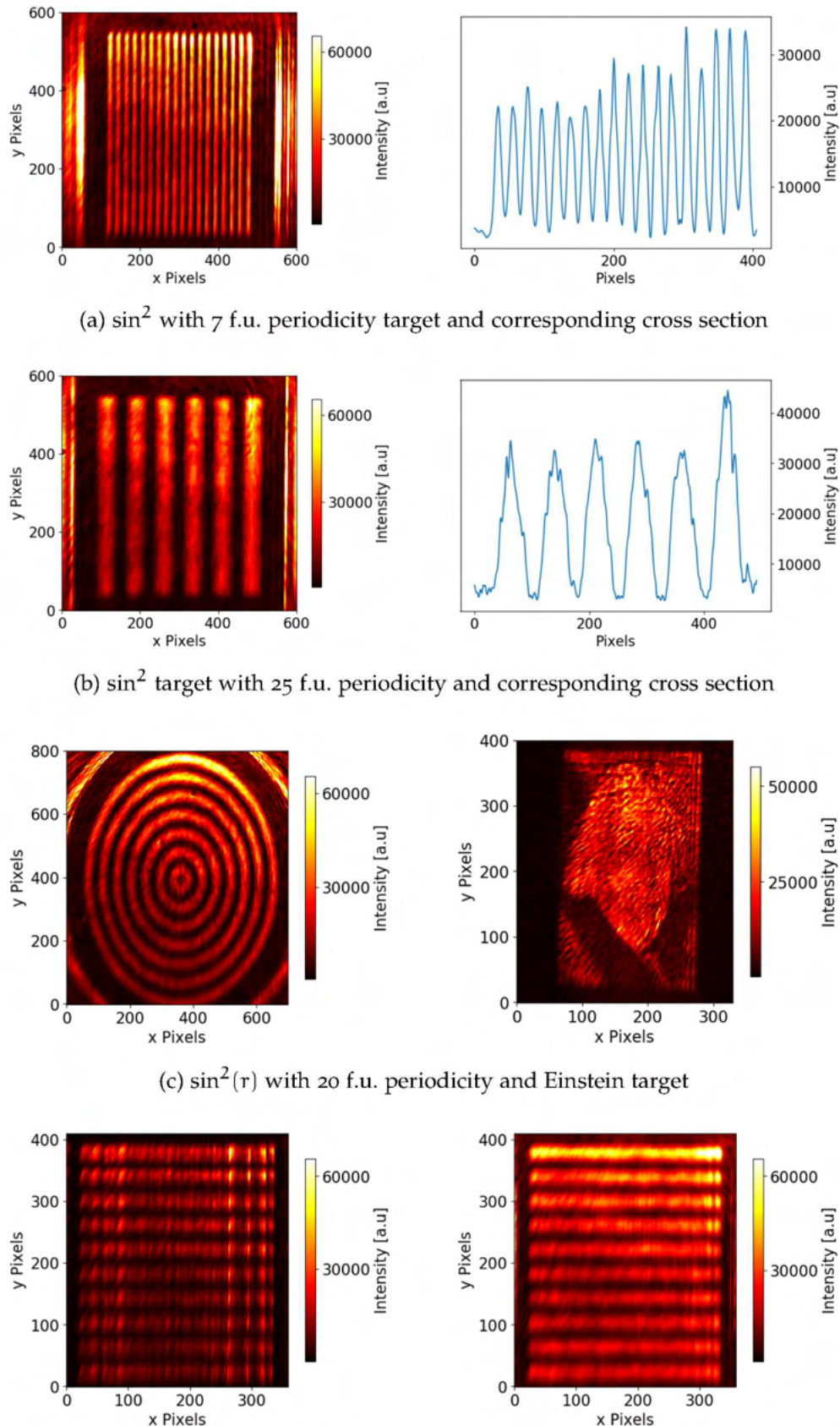


Figure 45: Excerpt of measured intensity patterns after spatially blocking the zero-order spot.

# 6

## CONCLUSION

---

### 6.1 SUMMARY

In this thesis preparatory work for a new approach to observing optical nonlinearities in a Rydberg gas has been pursued with the focus on beam shaping with a phase-modulating Spatial Light Modulator.

In order to create specific intensity patterns the first considerations were dedicated to computer-generated holography and how to calculate phase patterns that are needed for light to be shaped into a certain form in a Fourier-optical setup. This demand turns out to be an application of the phase retrieval problem, such that I could draw on the numerical method of iterative Fourier transform algorithms to solve it. Specifically the MRAF algorithm was implemented and tested. I was able to show that it does indeed produce good simulations for a variety of desired target intensities. In particular continuous periodical intensities as planned in the final Rydberg experiment could be simulated to an accuracy of a few percent error. For targets as required in our final experiment, which happen to be of a separable form, the phase pattern can be computed for each dimension separately, which theoretically yields slightly better simulations to the cost of light utilisation efficiency.

Concerning the experimental side of using the SLM, methods for correcting aberrations and proper beam alignment making use of the SLMs abilities have been presented and tested. The Shack-Hartmann algorithm was implemented and contributed to remove large scale aberrations, it could also be used in order to reconstruct the input intensity in the SLM plane. Thanks to the correction patterns and the correct beam specifications, the laser beam was shaped into sinusoidal targets. Nonetheless, first measurements showed that still errors persist, such that in practice we cannot reach the smooth intensity distributions as theoretically simulated. The influence of the light that cannot be modulated by the SLM was larger than assumed, towards the end of this project a simple method to filter out this error source was implemented.

During the project multiple avenues with ample potential for improvement have been identified. Implementing these shows marked promise towards achieving the desired pattern quality. Hence, the last

section of this thesis is dedicated to the presentation of these potential enhancements.

## 6.2 OUTLOOK

The ideas I propose for the consecutive work can be roughly divided into two sections. First, addressing issues that concern the actual setup, and second rethinking the way how the phase patterns are calculated.

### 6.2.1 Recalibrating the setup

Although I presented a way to correct aberrations with the SLM, the correction can probably be further improved. A simple indicator for this is the diffraction pattern of the SLM without any specific phase. Even after adding the measured correction patterns the shape is far from being perfectly  $\text{sinc}^2$  as the Fourier-transform of a rectangular aperture predicts (see figure 11). Furthermore the grid patterns that were made visible after aberration correction are still not optimal (see figure 36), some aberrations seem to remain.

The Shack-Hartmann algorithm is a first approach, but there are also other methods that sound more rewarding. Another type of aberration measurement might be of use in the future, namely *Phase-shifting interferometry* originally proposed by *Bruning et al.* [42], which makes use of the specific interference pattern of two beams. A thorough discussion of this technique and how to successfully adapt it to SLMs for aberration correction has been done by *Palm* [9] and *Hammel* [28]. The interference of two beams can be realized with a SLM by taking light from the centre of the SLM as a reference beam and light from another part as a probe beam (see figure 46). With at least three different phase measurements for each SLM sample the phase aberration  $\phi_A$  can be reconstructed. According to their results this method should provide a significantly more accurate way of addressing the aberrations. It is reported that in comparison the Shack-Hartmann algorithm is only able to correct large scale aberrations.

Hence, I suggest to implement it in our program and compare it to the Shack-Hartmann technique with regard to some phase-error-metrics. It might turn out that the image quality can improve further using PSI, if it is also able to reduce small scale aberrations as has been reported. It would be also interesting to see if the correction patterns measured with that method are also still valid when large linear phase gradients are applied to the SLM in order to shift the target. With the Shack-Hartmann correction phase patterns this does not seem to be the case.

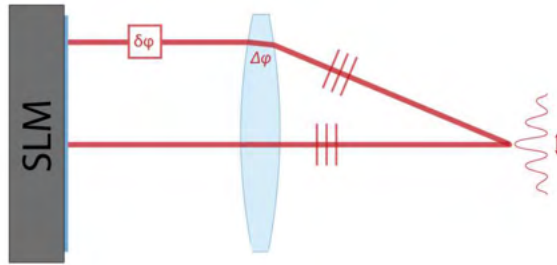


Figure 46: Phase-shifting Interferometry applied to SLMs, analysing the interference pattern of two beams originating from the SLM yields the local  $\phi_A$ , from [9]

Furthermore, it is obvious that the zero-order spot must be tamed. Currently it makes it difficult to distinguish between the different sources of errors that arise in the setup and therefore a suitable routine to filter out the zero-order spot needs to be found. The new setup I have built can serve as a basis for further investigations. At least here the strong intensity in the zero-order spot was not present anymore, which allowed for creating images with a stronger laser power, but it seems like the large linear gradients used also introduce additional noise, which is degrading the target quality. The large linear gradients are currently necessary because it seems like the zero-order spot has a wide-ranging influence in form of a destructive interference pattern. The latter is surprising because even though many publications mention the zero-order spot, the reports do not give the impression that the influence is that large. In order to improve removal of the zero-order it should be examined if adding quadratic phase patterns to the SLM can help for blocking it and also diminish the long ranging influence. This work has to be thoroughly documented, because the eventually added phase patterns will consequently have to be considered in all subsequent phase pattern calculations. Most publications only mention the zero-order spot briefly and do not go into detail about how they filtered it out. It is thus not clear how big the zero-order influence initially was in their setup. Removing the zero-order spot seems to be an experimental routine a group has to develop for itself. To that end some publications that only deal with eliminating the zero-order spot like [41] may help. Here a combination of linear and quadratic phase gradients is suggested.

In addition I recommend to check the entire current setup guiding the beam towards the SLM and the laser beam itself. If one carefully analyses the beam and its polarisation after each piece of the setup it might turn out that at some points major defects are introduced that we have so far overlooked. At least the amplitude reconstruction measurements in the SLM plane hints towards some impurities that

were reproducible (see figure 39a), although this could also be caused by the measurement method itself. The assumption of a continuous input intensity is important for the phase pattern calculations to be good. Most importantly the positioning of the SLM should be reconsidered. It could be investigated, how the incident angle affects the images, since we may not be using the optimal angle currently. In retrospect, this analysis of the setup should have been the first task. This revisiting of the setup with devices to measure beam profile and polarisation can be expensive and tedious, but I think that it is a valuable task. The experiences there might save a lot of time for the migration of the SLM into the final Rydberg gas experiment.

Finally, concerning the setup it should also be considered what the objective in the final experiment will implicate for the targets and how the resolution of the sinusoidal targets will be affected. The specific size specifications of the final experiment are also important for the phase pattern calculations, such that not too large or too small targets are simulated, the former causing unnecessary waste of light.

Lastly, one can still think about implementing a camera feedback method, which is probably the first correction method that comes to ones mind, but that requires some precise work in practice. Simple concepts for that kind of feedback have been presented e.g. in [8, 10, 43]. In principle they all consist of comparing desired target and actual image, adjusting the desired target and calculating a new phase pattern. As a correct mapping between camera image and target intensity has to be done, one has to be careful to not add some additional errors, but in the end this kind of feedback can be the most rewarding, possibly being a stand-alone method for all kind of errors without further aberration algorithm being needed. Implementing this kind of feedback is probably facilitated if it is not applied continuously but calculated once in an external program. Note, that LabVIEW is probably not the best programming language for such image comparison. Nonetheless it is probably more favourable, if the setup optimisation I proposed before turns out to be sufficient, so that such a program does not need to be developed.

### 6.2.2 *Rethinking beam shaping*

The second big task consists of reviewing the technique used to calculate the phase patterns.

Simulations with an IFTA are easy to implement, applicable for all kind of targets and in addition to their versatility are also very accurate. This is why they have established themselves as a robust method for shaping specific 2D traps and potentials. The fact that IFAs are so

widely used for this purpose made us believe that they are also suited for our purposes, although the phase in the image plane might be a constraint that we cannot allow to be a degree of freedom as the IFTA does.

This is due to the fact that the phase might cause some unwanted diffraction throughout the propagation of the light pattern. As the Rydberg gas in the experiment will have a depth of  $\sim 100\mu\text{m}$  it should be investigated how the phase is diffracting the intensity distributions. We would like the intensity pattern to be robust and only altered due to the influence of the Rydberg medium. Still, this is only a assumption that needs to be investigated. In order to do this the propagation of the light through the Rydberg medium according to the paraxial propagation equation has to be studied, which has the form

$$i\partial_z E(\mathbf{r}_\perp, \mathbf{z}) = \left[ -\frac{\nabla_\perp^2}{2k} + U(\mathbf{r}_\perp, \mathbf{z}) \right] E(\mathbf{r}_\perp, z) \quad (57)$$

where  $U(\mathbf{r}_\perp, z)$  is the effective light potential depending of the first and third order susceptibility:

$$U(\mathbf{r}_\perp, z) = \chi^{(1)}(\mathbf{r}_\perp, z) + \int \chi^{(3)}(\mathbf{r}_\perp - \mathbf{r}'_\perp) |E(\mathbf{r}'_\perp, z)|^2 d\mathbf{r}'_\perp \quad (58)$$

This equation is not solvable analytically but can be solved numerically using the split-step Fourier method as described in [3].

In principle we could simply plug the simulated patterns from the MRAF into this numerical simulation, including the phase in the image plane as another result of the IFTA that we have so far neglected. If the diffraction is too strong one could then recompute a similar good intensity pattern with another initial phase guess to get another phase distribution in the image plane. Nonetheless this straightforward trial and error approach might not produce satisfactory results at all. Therefore I suggest considering alternative ways of beam shaping, where also a phase is set as an additional constraint. Therefore the phase which is at least causing diffraction needs to be determined.

Setting a phase constraint is simply not possible with an IFTA, although it is actually conceivable to set a phase constraint only in a certain domain for instance (or some other type of soft constraint), but to my knowledge this has not been tried so far and there might be mathematical reasons that I am not aware of why adapting the IFTA like this would render it useless, but at least this could be tested once.

Fortunately, there are some other ways of phase pattern calculation where the phase in the image plane can be set, like the technique of analytic beam shaping briefly presented in section 3.3. In general analytic beam shaping only consists of one Fourier transform and thus also requires that the amplitude in the SLM plane can be

changed. The trick used to make this possible with phase-only modulating SLMs is to mimic a blazed grating. Locally changing the depth of this blazed grating can be used to also effectively manipulate the phase to the cost of a smaller light utilization efficiency compared to the MRAF. There is not a unique way to proceed for this, one of them has been intensively studied in [28] and a recent very interesting review paper [27] presents six of these methods. These techniques should be tested with regard to their ability to produce the desired targets but additionally also with regard to their ability to create the desired phase patterns in the image plane, something that the mentioned publications have not investigated. Of course the recreation of a desired intensity pattern is the first priority, but how a certain phase is reproduced would also be an interesting subject.

Analytic beam shaping with blazed gratings is not the only way of beam shaping where the phase can be set as a constraint. Another totally different and also algorithmic approach is the new method of conjugate gradient minimisation as presented by *Harte* [44]. This method functions on the basis of minimising cost functions and is thus mathematically more challenging than an IFTA, but nowadays enough numerical libraries exist to implement such a differential approach. The cost function can be adapted to one's needs and can also include the phase as a constraint as used by *Palm* [9], which is the reason why this approach should also be suited for simulating both amplitude and phase.

Additionally two other points might be of interest in the future concerning the calculation of the phase patterns.

A recent publication [36] recommends to optimize phase pattern calculations by making use of the full Helmholtz propagator and not only the Fourier transform. According to the authors this significantly improves the resulting images in an SLM setup.

Up to now the speed of the calculations was of no concern as in our experiment the phase patterns can simply be calculated in advance. If live calculation is desired, analytical beam shaping is probably the fastest method as long as the algorithmic approaches are not GPU accelerated, but at that point the limited refresh rate of the SLM (120Hz) is probably the most limiting factor (That is not the case for other types of SLMs like Digital Mirror Devices.). Eventually the light utilization efficiency of the beam-shaping methods is also of interest, probably not for the planned interaction imaging experiment, but for other types of setup where the available laser power is limited.

### 6.2.3 Closing remarks

Apart from finding the most suitable way of beam-shaping for our necessities, the workflow around the SLM should be reconsidered. At this early stage the investigations have relied on working with the LabVIEW-environment. LabVIEW makes programming accessible and the creation of GUIs easy. For controlling the SLM the current program is a reliable tool.

Nevertheless, it might be more productive to specify the tasks and outsource some of them into other more suited programming environments, for instance the implementation of different phase pattern calculations methods or image analysis (e.g. ImageAlign in Mathematica). Developing such a strategy of separating the tasks would keep the LabVIEW control program foreseeable, such that it is easier to adapt for other applications in the future without having to rewrite the entire LabVIEW-program. Furthermore, that would also enable more people with a diverse programming background to get involved into working with the SLM. This can only be beneficial for the project.

The phase-modulating SLM is a versatile tool on many different levels. Not only can it be used for all kinds of applications in atomic physics, but also allows for ideas and techniques coming from completely different fields to be applied to it, as exemplified by the aberration-correction methods for instance. The SLM is a device that invites scientists to be creative and tweak it to their needs.

Tackling the problems outlined above is not rocket science. Most of the required knowledge is already there, sometimes hidden in plain sight.

Taken as a whole, mastering light shaping with an SLM is just one step, but a very crucial one, towards observing the intricacies of optical non-linearities in a Rydberg gas and will for sure also render experiments possible that quantum physicists have not even thought of yet.



## BIBLIOGRAPHY

---

- [1] Thomas S Kuhn. *The Structure of Scientific Revolutions*. 1962.
- [2] T Pohl, CS Adams, and HR Sadephpour. "Cold Rydberg gases and ultra-cold plasmas". In: *Journal of Physics B: Atomic, Molecular and Optical Physics* 44.18 (2011), p. 180201.
- [3] Annika Tebben. "Resonant Enhancement of the Optical Nonlinearity in a Rydberg Gas". MA thesis. University of Heidelberg, 2018.
- [4] Theodore H Maiman et al. "Stimulated optical radiation in ruby". In: (1960).
- [5] Dennis Gabor. *A new microscopic principle*. 1948.
- [6] David G Grier. "A revolution in optical manipulation". In: *nature* 424.6950 (2003), p. 810.
- [7] David McGloin, Gabriel C Spalding, H Melville, Wilson Sibbett, and Kishan Dholakia. "Applications of spatial light modulators in atom optics". In: *Optics Express* 11.2 (2003), pp. 158–166.
- [8] Rick Martinus Wilhelmus van Bijnen. "Quantum engineering with ultracold atoms". PhD thesis.
- [9] Lukas Palm. "Exploring fractional quantum hall physics using ultracold fermions in rotating traps". MA thesis. University of Heidelberg, 2018.
- [10] Marvin Holten. "Hamiltonian Engineering in Ultracold Atom Experiments using a Spatial Light Modulator". B. Sc. Thesis, University of Heidelberg, 2014.
- [11] TF Gallagher. "Rydberg atoms". In: *Reports on Progress in Physics* 51.2 (1988), p. 143.
- [12] Stephen E Harris. "Electromagnetically induced transparency". In: *Physics Today* 50 (1997), pp. 36–42.
- [13] Michael Fleischhauer, Atac Imamoglu, and Jonathan P Marangos. "Electromagnetically induced transparency: Optics in coherent media". In: *Reviews of modern physics* 77.2 (2005), p. 633.
- [14] Jonathan D Pritchard, Kevin J Weatherill, and Charles S Adams. "Nonlinear optics using cold Rydberg atoms". In: *Annual Review of Cold Atoms and Molecules: Volume 1*. World Scientific, 2013, pp. 301–350.
- [15] K-J Boller, A Imamoğlu, and Stephen E Harris. "Observation of electromagnetically induced transparency". In: *Physical Review Letters* 66.20 (1991), p. 2593.

- [16] Lene Vestergaard Hau, Stephen E Harris, Zachary Dutton, and Cyrus H Behroozi. "Light speed reduction to 17 metres per second in an ultracold atomic gas". In: *Nature* 397.6720 (1999), p. 594.
- [17] Robert W Boyd. *Nonlinear optics*. Elsevier, 2003.
- [18] Joseph W Goodman. *Introduction to Fourier optics*. Roberts and Company Publishers, 2005.
- [19] Michael J Stephen and Joseph P Straley. "Physics of liquid crystals". In: *Reviews of Modern Physics* 46.4 (1974), p. 617.
- [20] Siegfried Hunklinger. *Festkörperphysik*. Oldenbourg Verlag, 2009.
- [21] Hamamatsu. *LCOS-SLM (Optical Phase Modulator) X10468-02*. URL: <https://www.hamamatsu.com/eu/en/product/type/X10468-02/index.html>.
- [22] Darwin Palima Jesper Glückstad. *Jones Calculus in Phase-Only Liquid Crystal Spatial Light Modulators*. URL: [https://cds.cern.ch/record/1339560/files/978-90-481-2839-6\\_BookBackMatter.pdf](https://cds.cern.ch/record/1339560/files/978-90-481-2839-6_BookBackMatter.pdf).
- [23] R.W. Gerchberg and W.O. Saxton. "A Practical Algorithm for the Determination of Phase from Image and Diffraction Plane". In: *Optik* (1972).
- [24] James R Fienup. "Phase retrieval algorithms: a comparison". In: *Applied optics* 21.15 (1982), pp. 2758–2769.
- [25] Harald Aagedal, Michael Schmid, Sebastian Egner, Jörn Müller-Quade, Thomas Beth, and Frank Wyrowski. "Analytical beam shaping with application to laser-diode arrays". In: *JOSA A* 14.7 (1997), pp. 1549–1553.
- [26] Matthew Pasienski. "Transport Properties of Ultracold Atoms in a Disordered Optical Lattice". PhD thesis. 2011.
- [27] Thomas W Clark, Rachel F Offer, Sonja Franke-Arnold, Aidan S Arnold, and Neal Radwell. "Comparison of beam generation techniques using a phase only spatial light modulator". In: *Optics express* 24.6 (2016), pp. 6249–6264.
- [28] Tobias Hammel. "Analytical approach to holography for robust trapping of ultracold atoms". B. Sc. Thesis, University of Heidelberg, 2019.
- [29] James R Fienup. "Phase retrieval algorithms: a personal tour". In: *Applied optics* 52.1 (2013), pp. 45–56.
- [30] Matthew Pasienski and Brian DeMarco. "A high-accuracy algorithm for designing arbitrary holographic atom traps". In: *Optics express* 16.3 (2008), pp. 2176–2190.
- [31] Hiroshi Akahori. "Spectrum leveling by an iterative algorithm with a dummy area for synthesizing the kinoform". In: *Applied optics* 25.5 (1986), pp. 802–811.

- [32] Les Allen, Marco W Beijersbergen, RJC Spreeuw, and JP Woerdman. "Orbital angular momentum of light and the transformation of Laguerre-Gaussian laser modes". In: *Physical Review A* 45.11 (1992), p. 8185.
- [33] Frank Wyrowski and Olof Bryngdahl. "Iterative Fourier-transform algorithm applied to computer holography". In: *JOSA A* 5.7 (1988), pp. 1058–1065.
- [34] Paramasivam Senthilkumaran, Frank Wyrowski, and Hagen Schimmel. "Vortex stagnation problem in iterative Fourier transform algorithms". In: *Optics and Lasers in Engineering* 43.1 (2005), pp. 43–56.
- [35] Harald Aagedal, Michael Schmid, Thomas Beth, Stephan Teiwes, and Frank Wyrowski. "Theory of speckles in diffractive optics and its application to beam shaping". In: *Journal of modern optics* 43.7 (1996), pp. 1409–1421.
- [36] Alexander L Gaunt and Zoran Hadzibabic. "Robust digital holography for ultracold atom trapping". In: *Scientific reports* 2 (2012), p. 721.
- [37] RMW van Bijnen, C Ravensbergen, DJ Bakker, GJ Dijk, SJM Kokkelmans, and EJD Vredenbregt. "Patterned Rydberg excitation and ionization with a spatial light modulator". In: *New Journal of Physics* 17.2 (2015), p. 023045.
- [38] Richard W Bowman, Amanda J Wright, and Miles J Padgett. "An SLM-based Shack-Hartmann wavefront sensor for aberration correction in optical tweezers". In: *Journal of Optics* 12.12 (2010), p. 124004.
- [39] Vasudevan Lakshminarayanan and Andre Fleck. "Zernike polynomials: a guide". In: *Journal of Modern Optics* 58.7 (2011), pp. 545–561.
- [40] Virendra N Mahajan and Guang-ming Dai. "Orthonormal polynomials in wavefront analysis: analytical solution". In: *JOSA A* 24.9 (2007), pp. 2994–3016.
- [41] Hao Zhang, Jinghui Xie, Juan Liu, and Yongtian Wang. "Elimination of a zero-order beam induced by a pixelated spatial light modulator for holographic projection". In: *Applied optics* 48.30 (2009), pp. 5834–5841.
- [42] J Herriot Brunning, Donald R Herriott, JE Gallagher, DP Rosenfeld, AD White, and DJ Brangaccio. "Digital wavefront measuring interferometer for testing optical surfaces and lenses". In: *Applied optics* 13.11 (1974), pp. 2693–2703.

- [43] Graham D Bruce, Matthew YH Johnson, Edward Cormack, David AW Richards, James Mayoh, and Donatella Cassettari. "Feedback-enhanced algorithm for aberration correction of holographic atom traps". In: *Journal of Physics B: Atomic, Molecular and Optical Physics* 48.11 (2015), p. 115303.
- [44] Tiffany Harte, Graham D Bruce, Jonathan Keeling, and Donatella Cassettari. "Conjugate gradient minimisation approach to generating holographic traps for ultracold atoms". In: *Optics Express* 22.22 (2014), pp. 26548–26558.